

Dissertation
submitted to the
Combined Faculties for the Natural Sciences and for Mathematics
of the Ruperto-Carola University of Heidelberg, Germany
for the degree of
Doctor of Natural Sciences

Put forward by
Diplom-Physiker Roman Schmidt
born in Wuppertal, Germany
Oral examination: November 5th, 2008

3D fluorescence microscopy with isotropic resolution on the nanoscale

Referees:

Prof. Dr. Stefan W. Hell
Prof. Dr. Christoph Cremer

Kurzdarstellung.

Die Auflösung eines jeden linearen Abbildungsverfahrens ist durch seine Punktbildfunktion (engl. point-spread-function, PSF) gegeben, die das Verwaschen eines Punktes des Urbilds quantifiziert. Je schärfer die PSF, desto besser die Auflösung. In der herkömmlichen Fluoreszenzmikroskopie weist die PSF beugungsbedingt ein zigarrenförmiges Hauptmaximum auf, welches auch fokaler Fleck genannt wird. Seine Ausdehnung beträgt mindestens die Hälfte der Lichtwellenlänge ($\lambda = 400\text{-}800\text{ nm}$) in der Fokalebene und $> \lambda$ entlang der optischen Achse (z). Obwohl Konzepte entwickelt wurden, die den fokalen Fleck sowohl lateral als auch axial schärfen, ist es bisher keinem von ihnen gelungen, das ultimatives Ziel zu erreichen: Die isotrope Abbildung mittels eines kugelförmigen fokalen Flecks, der beliebig verkleinert werden kann. Hier stelle ich solch ein Fluoreszenzmikroskop vor und demonstriere die Erzeugung eines kugelförmigen fokalen Flecks mit einem Durchmesser von $40\text{-}45\text{ nm}$ ($\sim \lambda/16$), der unter geeigneten Bedingungen auf $21\text{-}30\text{ nm}$ ($\sim \lambda/30$) verkleinert wird. Rein auf fokussiertem Licht basierend, blickt dieses linsenbasierte Fluoreszenznanoskop in das Innere von Zellen und analysiert nicht-invasiv die Struktur ihrer sub- λ messenden Organellen. Weitere Anwendungen, wie zum Beispiel die Charakterisierung neuartiger Nanomaterialien, eröffnen neue Einsatzgebiete.

Abstract.

The resolution of any linear imaging system is given by its point-spread-function (PSF) quantifying the blur of an object point in the image. The sharper the PSF, the better is the resolution. In standard fluorescence microscopy, however, diffraction dictates a PSF with a cigar-shaped main maximum, called the focal spot which extends over at least half the wavelength of light ($\lambda = 400\text{-}800\text{ nm}$) in the focal plane and $> \lambda$ along the optic axis (z). While concepts have evolved to sharpen the focal spot both laterally and axially, none of them has reached their ultimate goal: a spherical spot that can be arbitrarily downscaled in size. Herein, I introduce such a fluorescence microscope and demonstrate the creation of spherical focal spots of $40\text{-}45\text{ nm}$ ($\sim \lambda/16$) diameter that is pushed down to $21\text{-}30\text{ nm}$ ($\sim \lambda/30$) under suitable conditions. Fully relying on focused light, this lens-based fluorescence nanoscope unravels the interior of cells non-invasively, uniquely dissecting their sub- λ sized organelles. Further fields of application open up, such as the characterization of novel nanomaterials.

Contents

1	Introduction	11
2	A spherical nanosized focal spot unravels the interior of cells	15
2.1	Coherence for a sharper image	15
2.1.1	PSF and OTF of 4Pi microscopy and I ⁵ M	18
2.2	The I ⁵ M/4Pi hybrid microscope	24
2.2.1	PSF-measurements	27
2.2.2	Comparative imaging of biological specimen.	29
2.2.3	Simulations	32
2.3	Pushing the limits of 4Pi microscopy and I ⁵ M	35
2.3.1	Objective lenses	35
2.3.2	Sample thickness and recording volume	36
2.4	isoSTED microscopy	39
2.4.1	STED augmented 4Pi microscopy	39
2.4.2	Spherical focal spot generation	41
2.4.3	Dual-color 3D nanoscopy imaging	49
2.4.4	isoSTED microscopy with a single depletion beam	51
2.4.5	Discussion and outlook	53
3	Spotlights on isoSTED application	57
3.1	Unfolding the blueprint of life	57
3.1.1	The Golgi apparatus	58
3.1.2	Mitochondria	60
3.2	Studies on the architecture of nanomaterials	62
A	Methods	67
B	Publications and presentations	69
	Bibliography	73
	Acknowledgment	81

List of Figures

1.1	Significance of isotropic superresolution.	13
2.1	Principles of I ⁵ M and 4Pi microscopy.	16
2.2	OTFs of 4Pi microscopy and I ⁵ M.	23
2.3	Experimental setup for I ⁵ M and 4Pi microscopy.	25
2.4	Progression of $F(\lambda)$ for 4Pi of Type C and I ⁵ M.	28
2.5	Experimental and theoretical PSFs of 4Pi microscopy and I ⁵ M.	30
2.6	Recordings of <i>E. coli</i> in 4Pi- and I ⁵ M-mode.	31
2.7	Removal of ghosting for different imaging modes.	33
2.8	Imaging properties of high-NA objective lenses in a 4Pi setup.	37
2.9	Progression of $F(\lambda)$ for STED-4Pi of Type C.	41
2.10	Performance of the STED-4Pi beam scanning microscope.	42
2.11	Fluorescence microscopy setup with isotropic 3D focal spot.	43
2.12	4Pi-module of the isoSTED microscope.	44
2.13	Formation of the isoSTED depletion PSF.	46
2.14	Isotropic effective focal spot (PSF) on the nanoscale.	48
2.15	isoSTED fluorescence microscopy dissects a mitochondrion.	50
2.16	Two-color isoSTED imaging of mitochondria in Vero cells.	52
2.17	isoSTED-sdb microscope and PSF generation.	54
2.18	Experimental isoSTED-sdb PSF and imaging in the nucleus.	55
3.1	Sub-structure of the Golgi apparatus.	59
3.2	Spatial distribution of mitochondrial proteins.	61
3.3	Non-invasive 3D imaging of PS-P2VP nanostructure.	64

1 Introduction

Far-field fluorescence microscopy is exceptional in its ability to non-invasively image the interior of cells with molecular specificity and in three dimensions (3D). However, for many decades, the resolution of its standard variants have been limited by a main point spread function (PSF) maximum having a cross-sectional diameter of > 200 nm in the focal plane (x,y) and a length of > 500 nm along the optic axis (z). To overcome these limits, microscopy concepts emerged to shrink the effective spot in size. By coherently adding the spherical wavefronts of two opposing lenses, 4Pi microscopy^{1,2,3,4} and I⁵M⁵ have reduced the main maximum of the PSF by a factor of 3-7 along the optic axis. A more fundamental reduction has been attained by exploiting molecular transitions of the fluorophore specifically for this purpose^{6,7}. For example, in STED (stimulated emission depletion) microscopy⁸, the main PSF extent is decreased to a small fraction of the wavelength, λ , by overlapping the spot of excitation light with a light distribution that features a local intensity zero to quench the excited fluorophores everywhere except at the zero. Thus the spot of effective fluorophore excitation is essentially confined to the proximity of the zero. All labels falling within the volume of the PSF maximum can contribute to the signal at the same time. When implemented in a scanning microscope, the subdiffraction-sized PSF yields images with subdiffraction resolution^{9,10}.

Intriguingly, any fluorophore process that reversibly inhibits fluorescence generation can be utilized to break the diffraction barrier^{6,7}. Therefore, related schemes have utilized other intramolecular fluorophore transitions to squeeze the focal spot and hence to sharpen the PSF, such as the depletion of the fluorophore ground state^{11,12}, or the switching of photochromic molecules between a fluorescence activated 'on' and a deactivated 'off' state¹³. The sharpening of the focal spot by PSF engineering^{6,7} is equivalent to expanding the microscope's spatial frequency pass-band. This can also be achieved in highly parallelized recording schemes that narrow the PSF with arrays of zeros¹⁴. Molecular switching has also opened the door to powerful superresolution schemes that switch photochromic molecules individually in a widefield illumination microscope, so as to mathematically localize them through the bunch of photons emitted in the 'on' state^{15,16,17,18}. These concepts utilize, and in fact rely on the assumption of switching on a single molecule at a time in the diffraction volume. While an impressive simultaneous gain in lateral and axial resolution

has recently been demonstrated¹⁹, obtaining such images has so far required fluorophores that are both switchable and exceptionally bright. Moreover, since the object is read out molecule by molecule, this approach has to avoid background signal from the body of the cell. Therefore superresolving by single molecule switching, as opposed to that by PSF engineering^{6,7}, has so far been limited to thin object layers that are close to the cover slip¹⁹. Although the resolution increase provided by single molecule switching concepts can be extended to the z-axis¹⁹, they inherently lack 3D optical sectioning, unless they are combined with multiphoton excitation²⁰.

The need for imaging deep inside a cell leaves ensemble methods and hence the sharpening of the PSF^{6,7} highly attractive. Spot or multiple spot oriented schemes are applicable to normal (non-switchable) fluorophores, and by detecting molecular ensembles, they allow the tuning of the signal strength by varying the spot size. The latter is particularly important for the nanoscale imaging inside living cells²¹. In conjunction with confocal detection, they effectively suppress the background which renders them single molecule sensitive. Last but not least, directing the focal spot to an arbitrary coordinate in the sample enables direct probing of sites of interest in the cellular interior. However, to unfold its full 3D imaging potential, the PSF must be spherical; in fact, one can argue that the 3D-resolution is limited by its weakest part (**Fig. 1.1**). Unfortunately, due to the highly asymmetric convergence of the focused wavefront at the focal point of a lens, isotropic focal spots are not readily attained.

In this thesis, I demonstrate a solution to this problem by encircling the focal point of a scanning fluorescence microscope by a focal intensity distribution that depletes the potentially excited molecules by stimulated emission. *“A spherical nanosized focal spot unravels the interior of cells”* discusses the design and development of the isoSTED microscope that implements this concept. The net result is an effective PSF delivering a virtually isotropic spatial resolution of 40-45 nm ($\sim \lambda/16$) that can be pushed down to 21-30 nm ($\sim \lambda/30$) under suitable conditions. As an initial study, multicolor 3D nanoscale imaging of mitochondria in morphologically intact fixed mammalian cells reveals that although the mitochondrial protein Tom20 clearly delineated the mitochondrial outer membrane, Tom20 is predominantly assembled in clusters. *“Spotlights on isoSTED application”* further exemplifies the potential of non-invasive 3D nanoscopy to progress current topics in the life- and material sciences.

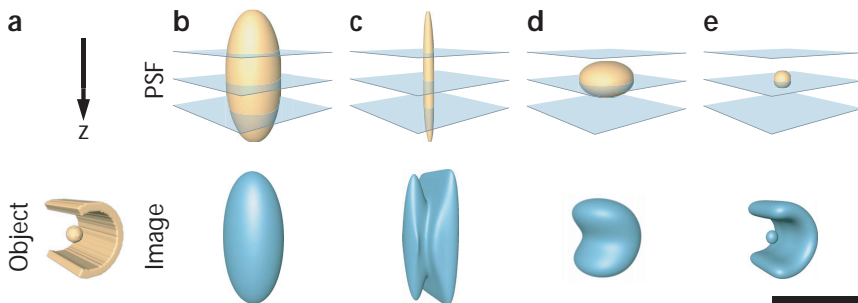


Figure 1.1: Significance of isotropic superresolution. The resolving power of an imaging system is generally defined by its point spread function (PSF), i.e. the image one would obtain from measuring a point-object. The image of an arbitrary object can then be described mathematically as a convolution of the object with the PSF of the instrument. Object variations in space that are larger than the PSF will show up nicely, while those that are much smaller will be blurred beyond recognition. Therefore, a microscope's ability to resolve complex 3D objects strongly depends on its resolution along its weakest direction, i.e. the direction along which the PSF extends the furthest. (a-e) To illustrate this, the image of an object made up of a tube of 200 nm outer diameter containing a 50 nm sphere at its center (a) has been calculated for different PSFs. If the object is imaged with a confocal microscope (b, $\text{FWHM}_{xy} = 160$ nm, $\text{FWHM}_z = 380$ nm), it is not possible to resolve any features. An increase in lateral resolution^{22,23,24,25} amplifies the prolate shape of the PSF (c, $\text{FWHM}_{xy} = 30$ nm, $\text{FWHM}_z = 380$ nm). Although the gain in resolution visualizes features that were not observable before, the comparatively poor z-resolution misses out essential details. Increasing the resolution along the axial direction^{2,5,3,10,26} mainly results in an oblate shaped PSF (d, $\text{FWHM}_{xy} = 160$ nm, $\text{FWHM}_z = 100$ nm). Such microscopes reproduce the object's overall shape quite nicely although the fine details are still lost during the imaging process. Only an isotropic nano-sized focal spot (e, $\text{FWHM}_{xy} = 50$ nm, $\text{FWHM}_z = 50$ nm) is able to retrieve the object's full 3D information. The isosurfaces were calculated for 50 % of the peak intensity. Scale bar, 250 nm.

2 A spherical nanosized focal spot unravels the interior of cells

With the advent of molecular switching mechanisms in high resolution microscopy, biological nanoscale imaging became a reality. However, the number of switching cycles that a fluorophore can undergo until it becomes inactive is usually finite. Sharpening the focal spot therefore demands carefully engineered light fields to keep exposure of those parts of the sample that are not read out at a minimum. Because of the technical challenges involved, sharpening of the PSF used to be confined to one or two dimensions, leading to highly unisotropic PSFs. Imaging was thus limited to more or less two-dimensional samples, that exhibited no complex 3D-structure.

To enable 3D nanoscopy of complex samples, this study initially centers around 4Pi microscopy and I⁵M, those two closely related techniques that succeeded in reducing the axial focus dimensions substantially. The development of an I⁵M/4Pi-hybrid microscope allowed thorough investigation and comparison of both techniques. The lessons learned about their individual strengths and weaknesses helped to identify a promising microscope design for finally pushing the resolution far beyond the diffraction limit. STED augmented 4Pi microscopy pioneered the utilization of molecular switching mechanisms in a complex beam scanning setup, thus paving the way for the development of the isoSTED microscope that realises the nanosized spherical focal spot.

2.1 Coherence for a sharper image

4Pi and I⁵M fluorescence microscopy rely on the coherent addition of spherical wavefronts of two opposing high aperture angle lenses to provide an axial (z) resolution of ~ 100 nm, an about 5-fold improvement over conventional confocal microscopy.

4Pi microscopy

In 4Pi microscopy, the sample is illuminated by focusing excitation light through both objective lenses in a coherent manner onto the same spot and/or by coherently detecting the emerging fluorescence light through both lenses (**Fig. 2.1a**).

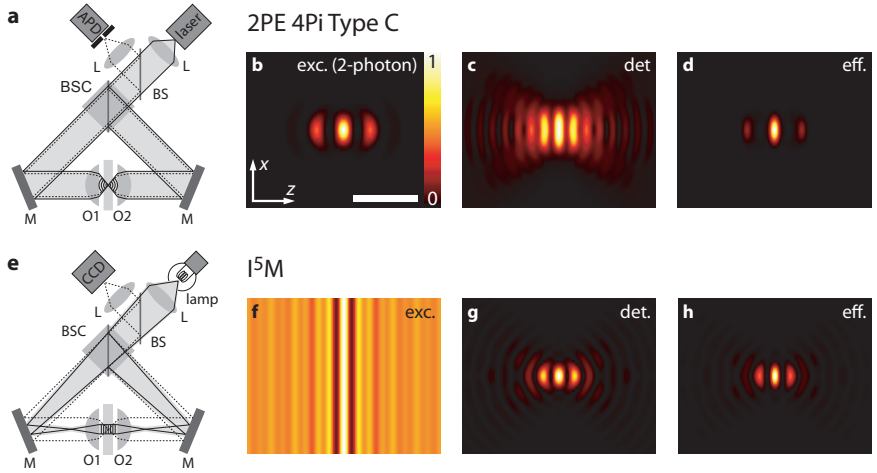


Figure 2.1: Principles of I⁵M and 4Pi microscopy. Scheme of (a) 2PE 4Pi microscopy of Type C and (e) I⁵M with the corresponding (b,f) excitation-PSFs, (c,g) detection-PSFs and (d,h) effective PSFs. The color tables are normalized to maximum intensity, their minima correspond to zero intensity. The visibility of weak intensities is enhanced by the color gradient. The calculations were performed for a semi-aperture angle of 1.12 rad. The broadening of the 4Pi detection-PSF (c) is due to the pinhole size of one Airy-disk diameter at the detection wavelength of 510 nm. Excitation wavelengths of 870 nm and 480 nm were assumed for 2PE 4Pi and I⁵M, respectively. Scale bar, 1 μ m.

Being equivalent to an increase in the aperture of the system, the constructive interference of the two focused light fields produces an illumination/detection PSF which features a central peak that is about 3-4 times narrower than the focal spot of a single lens with the largest aperture angle available (**Fig. 2.1b,c**). In the two-photon excitation (2PE)^{27,28} 'Type C' mode of 4Pi microscopy^{2,4,29}, the fluorescence is collected by both lenses and the coherent superposition of these two lightfields is detected at a common point that is usually defined by a pinhole. With a proper phase difference (multiples of 2π) at the detector, the detection-PSF is modified much in the same way as the excitation-PSF (**Fig. 2.1c**). The resulting effective PSF of the system (**Fig. 2.1d**) features sidelobes that are $< 25\%$ ^{2,4} of the main maximum. An x-y-image is obtained by scanning either the sample or the beams.

I⁵M

In I⁵M, the laser is replaced by a spatially incoherent light source such as an arc lamp and the sample is preferably Köhler-illuminated via both objective lenses (**Fig. 2.1e**), thereby making x-y-scanning redundant^{30,31,5}. Ideally, an azimuthal polarizer in the pupil plane of the lenses polarizes the excitation light perpendicular to the radial direction. The interfering light produces a laterally homogenous axial interference pattern whose modulation rapidly decreases to a constant intensity outside the common focal plane of the lenses (**Fig. 2.1f**). The fluorescence is collected as in a 4Pi-microscope (of Type C), i.e. by combining the spherical wavefronts originating from a sample point in the focal plane and by subsequently adding them at the same point of detection, typically at a CCD camera. Combined with the described excitation pattern, the detection PSF (**Fig. 2.1g**) leads to an effective PSF as shown in **Fig. 2.1h**. The spherical wavefront detection imprints a spherical lobe structure in the effective PSF of the I⁵M.

The effective PSFs of both systems feature a sharp central spot of about 100 nm (full width at half maximum, FWHM) axial width accompanied by axially shifted side-maxima (**Fig. 2.1d,h**). Unfortunately, these sidelobes lead to invalid replications in the image, commonly referred to as 'ghost images' or 'ghosting'. The removal of these ghost images is crucial for an unambiguous interpretation of the recorded structure. The sharpening of the central spot of the PSF enlarges the optical transfer function (OTF) of the system correspondingly. However, the sidelobes in the PSF lead to dips^{5,32,4,26} within the region of support of the OTF. The spatial frequencies of the dips have to be subsequently amplified in the image to obtain axially superresolved images that are free from ghosting³³.

In a theoretical comparison³² it has been shown that the dips in the OTF of a 2PE 4Pi-microscope of any type are much less pronounced and also significantly

smoother than in the I⁵M, which greatly simplifies the frequency build-up. The reason for the superior OTF of the 4Pi system of Type C is the synergistic combination of three mechanisms for suppressing the sidelobes:

First, 2PE reduces the sidelobe height due to the quadratic dependence on the illumination intensity. Second, especially in the 2PE case, the confocal detection pinhole suppresses the sidelobes, since the sidelobes of the excitation light are shifted away from the focal plane due to the longer wavelength. Third, the simultaneous use of coherent excitation and detection aperture expansion takes advantage of the difference between the two wavelengths reducing the spatial overlap of the sidelobes of the excitation and the detection PSFs. Instead, the multiplication of the minima of one PSF with the maxima of the other lowers the sidelobes of the effective PSF.

Due to its widefield-approach, I⁵M can take advantage only of the latter. In 2PE 4Pi microscopy, however, this effect is much more pronounced due to the much larger shift between the excitation and detection wavelengths.

The difference between the OTFs of the two imaging techniques favours the 4Pi system, but I⁵M excels with a faster recording of the raw data. This is due to the fact that the degree of parallelization in the focal plane is inherently maximized in I⁵M, whereas parallelization in a 4Pi system still requires multiple foci³ that are spatially separated. The fact that more photons can be obtained from the sample with single-photon excitation (1PE) as compared to 2PE also favours the use of the I⁵M. Especially this last detail could improve the signal to noise ratio (SNR) of an I⁵M to a stage that compensates its inherent optical disadvantages, thereby making I⁵M the preferable option in the end.

2.1.1 PSF and OTF of 4Pi microscopy and I⁵M

The effective PSF $h(\mathbf{x})$ of a fluorescence microscope is a product of the excitation-PSF $h_{exc}(\mathbf{x})$, and the detection-PSF $h_{det}(\mathbf{x})$. Being the Fourier transform of the PSF, the complex OTF $H(\mathbf{k})$ is the convolution of the complex excitation-OTF $H_{exc}(\mathbf{k})$ and the corresponding detection-OTF $H_{det}(\mathbf{k})$.

Excitation-PSF and OTF in the 4Pi-mode.

The two objective lenses focus into the common focal point at $\mathbf{x} = 0$, where the two focal fields add up coherently:

$$h_{exc}^{4Pi}(\mathbf{x}) = |\mathbf{E}^{(1)}(\mathbf{x}) + \tilde{\mathbf{M}}\mathbf{E}^{(1)}(\tilde{\mathbf{M}}\mathbf{x})|^{2m} \quad (2.1)$$

with

$$\tilde{\mathbf{M}} = \begin{pmatrix} 1 & 0 & 0 \\ 0 & 1 & 0 \\ 0 & 0 & -1 \end{pmatrix}, \text{ constructive interference assumed.} \quad (2.2)$$

$\mathbf{E}^{(1)}(\mathbf{x})$ is the electric light field in the focus of a single lens^{34, 35}. The parameter $m = 1, 2$ is valid for 1PE and 2PE, respectively. The vectorial OTF of the 4Pi-illumination can be calculated as described elsewhere³⁶. For 2PE, the resulting OTF has to be convolved with itself to achieve the proper excitation OTF.

Excitation interference pattern and OTF in the I^{5M} mode.

In I^{5M}, a spatially incoherent light-source is used for excitation, preferably in the Köhler mode. Each point of the light source is focused into the pupils of the two objective lenses thus individually creating a standing wave. The set of standing waves are oriented parallel to the focal plane with a periodicity of $(\lambda_0/2n)/\cos(\theta)$ with λ_0 being the (vacuum) wavelength, and n the refractive index of the medium. The denoted θ is the angle between the wave vector of the interfering incident plane waves and the optic axis, it corresponds to the normalized radial position $r = \sin \theta$ ($r \geq 0$) of a point-source in the pupil. Due to the spatial incoherence of the light source, the standing waves matching the different points of the pupil of the same lens do not mutually interfere, rather their intensities add up incoherently. For zero phase difference between the interference arms and for x-polarized incident light in the pupil plane, this leads to the following intensity distribution in the region of the focal plane:

$$h_{exc}^{I5M}(\mathbf{x}) \equiv h_{exc}^{I5M}(z) \propto \int_0^{2\pi} d\phi \int_0^\alpha d\theta \sin \theta P(\phi, \theta) \left[\left\{ E_x^{(0)}(\phi, \theta)^2 + E_y^{(0)}(\phi, \theta)^2 \right\} \cos^2(k(\theta)z) + E_z^{(0)}(\phi, \theta)^2 \sin^2(k(\theta)z) \right] \quad (2.3)$$

with

$$k(\theta) = 2\pi \frac{n \cos(\theta)}{\lambda_0} \quad (2.4)$$

and

$$\mathbf{E}^0(\phi, \theta) = E^{(0)} \begin{pmatrix} \cos \theta \cos^2 \phi + \sin^2 \phi \\ -\cos \phi \sin \phi (1 - \cos \theta) \\ -\sin \theta \cos \phi \end{pmatrix} \quad (2.5)$$

where α is the semi-aperture angle of the objective lenses and $P(\phi, \theta)$ denotes the polarization-independent pupil function. For a rotational symmetric pupil function, the integral can be simplified to

$$h_{exc}^{I5M}(z) \propto \int_0^\alpha d\theta P(\theta) \left[\{ \sin \theta (\cos^2 \theta + 1) \} \cos^2(k(\theta)z) + \sin^3 \theta \sin^2(k(\theta)z) \right] \quad (2.6)$$

Substituting $\cos \theta = \rho$ this integral can be written as

$$h_{exc}^{I5M}(z) \propto \int_{\cos \alpha}^1 d\rho P(\rho) \left[\rho^2 \cos(2k(\rho)z) + 1 \right] \quad (2.7)$$

2 A spherical nanosized focal spot unravels the interior of cells

For specific pupil functions such as $P(\theta) = 1$ or $P(\theta) = \cos \theta$, this integral can be solved analytically. Fourier-transforming $h_{exc}^{I5M}(\mathbf{x})$ yields the OTF of the excitation

$$H_{exc}^{I5M}(\mathbf{k}) \propto \begin{cases} \delta(k_z) \int_{\cos \alpha}^1 d\rho P(\rho) + \frac{1}{4k_0} \frac{k_z^2}{4k_0^2} P(k_z/2k_0) & k_x = k_y = 0 \\ [\Theta(2k_0 - |k_z|) - \Theta(2k_0 \cos \alpha - |k_z|)] & \\ 0 & \text{else} \end{cases} \quad (2.8)$$

with $k_0 = 2\pi n/\lambda_0$ and $\Theta(k)$ denoting the unit-step function with $\Theta(k) = 0$ for negative k and $\Theta(k) = 1$ otherwise. This OTF consists of a central singularity and two sidebands modulated by the pupil function and defined between $2k_0 \cos(\alpha)$ and $2k_0$.

In the practical case of imaging, the recorded data will always be limited in space and will consist of a finite number of pixels, leading to a discretization in the Fourier space. The OTF-singularity becomes a single pixel with a finite volume corresponding to the total signal of the PSF in the given recording volume. Since the I^{5M} PSF is not spatially confined, this value clearly depends on the size of this volume. If the lateral dimensions are sufficiently large, such that the PSF is not truncated laterally, the value of the central pixel is proportional to the axial extent of the data set. In contrast, OTF-values at higher spatial frequencies converge with increasing axial recording size, since in regions far away from the focal plane any modulation by interference fades away. As a result, the non-zero spatial frequencies decrease in relation to the central peak. For the correct interpretation of the OTF of I^{5M} it is therefore important to pay attention to the size of the data set.

According to (2.3), for uniformly x-polarized light in the pupil plane, the z-component of the E-field in the focal region contributes with a \sin^2 to the intensity distribution, whereas the lateral E-field components create a \cos^2 -modulation. The z-component thus lowers the contrast of the modulation pattern and therefore decreases the weight of higher spatial frequencies in the OTF compared to the central singularity that corresponds to the average signal. This z-component can be avoided by using an azimuthal polarizer in the incident light beam⁵. In this case, (2.3) reduces to the scalar case, which differs from (2.7) and (2.8) only by a factor ρ^2 and $k_z^2/4k_0^2$, respectively:

$$h_{exc}^{I5M}(z) \propto \int_{\cos \alpha}^1 d\rho P(\rho) [\cos(2k(\rho)z) + 1] \quad (2.9)$$

$$H_{exc}^{I5M}(\mathbf{k}) \propto \begin{cases} \delta(k_z) \int_{\cos \alpha}^1 d\rho P(\rho) + \frac{1}{4k_0} P(k_z/2k_0) & k_x = k_y = 0 \\ [\Theta(2k_0 - |k_z|) - \Theta(2k_0 \cos \alpha - |k_z|)] & \\ 0 & \text{else} \end{cases} \quad (2.10)$$

Alternatively to using an azimuthal polarizer, for x-polarized light, a y-oriented slit aperture can be brought into the pupil plane, constricting the pupil function to angles $\phi = 90$ and $\phi = 270$ (see (2.5)). With the pupil function P adapted correspondingly, the radial intensity distribution can be compensated to restore the larger relative fraction of light at high aperture-angles.

In the calculation of the excitation interference pattern and OTF, it was assumed that the excitation light is monochromatic. A finite bandwidth of the illumination (corrected by the excitation cross-section of the used fluorophore at each wavelength) broadens the sideband in the OTF in the same way as a range of angles θ . Compared to the width of the sideband resulting from the large aperture angles of high-NA lenses, broadening due to spectral effects is negligible for typical dyes and is omitted in this calculation.

Detection-PSF and OTF in the 4Pi-mode.

In the used setup, the fluorescence light is collected by both objective lenses and coherently combined. In this 'Type C' realisation of 4Pi microscopy, the detection-PSF is calculated in the same way as the excitation-PSF. In contrast to the laser excitation, the fluorescence is only weakly polarized; in fact it is here simplified as non-polarized. The wavelength can be assumed to be monochromatic at the barycentre of the detected spectrum. To take the finite size of the pinhole into account, the PSF for a point-like pinhole $h_{det,point}(\mathbf{x})$ is convolved with the back-projected pinhole in the object space $d(\mathbf{x})$. For the OTF, this is equivalent to the multiplication of the OTF for a point-like pinhole $H_{det,point}(\mathbf{k})$ with an Airy-pattern $D(\mathbf{k})$ which is the Fourier-transform of the pinhole disc $d(\mathbf{x})$.

Detection-PSF and OTF in the I⁵M-mode.

In I⁵M-detection, the common focal plane is imaged through both lenses onto a CCD-camera. Each fluorescence molecule in the focal plane can be regarded as a point source emitting spherical wavefronts. Spherical segments of these wavefronts are collected by the (finite aperture angle of the) lenses and added coherently on the same pixel of the CCD camera, which is analogue to the detection pinhole in the 4Pi-microscope. Thus, in the I⁵M, the detection occurs in the same way as in a 4Pi microscope of Type C and the detection-PSFs are the same. The back-projected pixel size that corresponds to the pinhole size in 4Pi microscopy is of secondary importance. By changing the magnification in the detection path or by using a different CCD-camera, the back-projected

pixel size can be easily lowered to values much smaller than the diameter of the Airy disc without wasting any fluorescent light.

To describe the I⁵M, it is therefore reasonable to use the detection PSF of a point-like detector just like for 4Pi microscopy. However, this does not imply an enhancement of the lateral resolution as encountered in confocal and 4Pi microscopy, because the I⁵M lacks the lateral confinement provided by confocality or by 2PE.

Comparison of the effective PSFs and OTFs.

PSFs of the two microscopes are shown in **Fig. 2.1**. Due to the synergistic combination of 2PE, confocal detection, as well as the coherent use of the excitation and fluorescence light fields, the 2PE 4Pi-C-PSF features sidelobes of typically less than half the height of the I⁵M-PSF side-maxima. In contrast to 2PE 4Pi-C, the I⁵M-PSF is not separable into a product of one-dimensional functions³⁷. Hence a fast removal of the sidelobes by a simple (3-point) deconvolution along the z-axis^{38,32} is not possible.

Figure 2.2 displays the effective OTFs of 4Pi microscopy and I⁵M. In addition to the discussed 2PE-mode of 4Pi-C-microscopy, the OTF of 1PE 4Pi-C-microscopy is shown. For the calculations, excitation wavelengths of 480 nm, 870 nm and 488 nm were used for I⁵M, 2PE 4Pi-C and 1PE 4Pi-C-microscopy, respectively. The detection wavelength was set to 510 nm. The assumed semi-aperture angle of the objective lenses was 1.12 rad corresponding to the semi-aperture angle of the 1.20 NA water immersion lenses used in the experiments. For 4Pi microscopy, a pinhole diameter of one Airy disc at the fluorescence wavelength was assumed. For I⁵M-excitation, azimuthally polarized light with a uniform pupil function was chosen. Representing the case experimentally realized in this paper, the OTF for randomly polarized light and an aplanatic lens system was calculated as well.

Due to the missing spatial confinement of the I⁵M-PSF, the I⁵M-OTF features a singularity at its origin, representing the total signal of the I⁵M-PSF. The finite value at the origin of the displayed OTF (**Fig. 2.2e**) corresponds to a volume of $(\sim 9.6 \mu\text{m})^3$ considered for excitation and recording. To highlight the outer regions of the I⁵M-OTF, the inset (**Fig. 2.2e**) shows the same OTF normalized to 10 % of the maximum. From the profiles shown beneath the OTF panels (**Fig. 2.2**), the depth of the dips in the OTFs can be recognized. While in 2PE 4Pi-C-microscopy (**Fig. 2.2d**) the dips are at only 49.6 % of the central peak, in the 1PE version the dips decrease to nearly 4.5 % (**Fig. 2.2b**). In contrast, in I⁵M the dips are down to 0.6 % (**Fig. 2.2f**, inset). In the case encountered in the experiment, the minima are ~ 0.4 % (red dashed line in the inset of **Fig. 2f**). Note that the relative height of the minima in the I⁵M-OTF scales approximately inversely with the axial extent of the corresponding

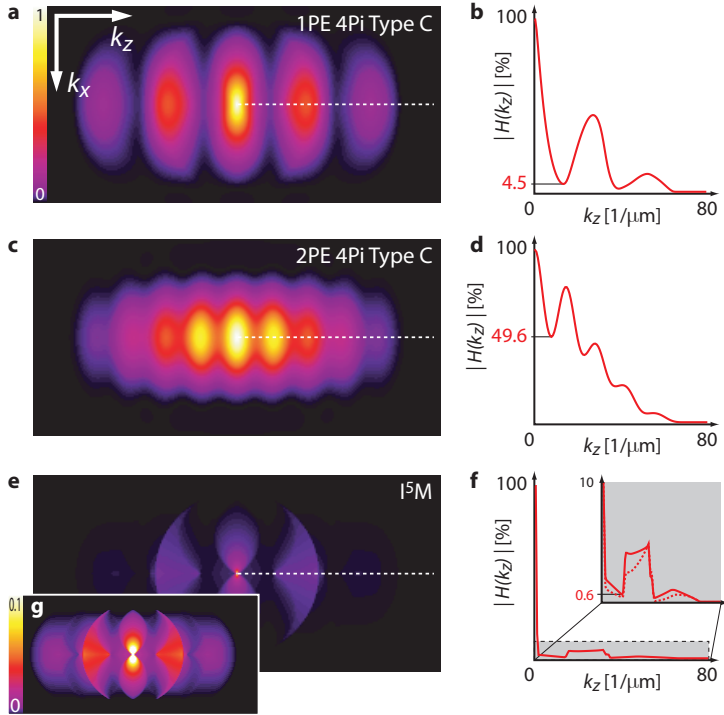


Figure 2.2: OTFs of 4Pi microscopy and I⁵M. The OTFs were calculated according to a vectorial theory assuming a semi-aperture angle of 1.12 rad. For excitation, 488 nm (a), 870 nm (c) and 480 nm (e) were used with a detection wavelength of 510 nm. A pinhole diameter corresponding to one Airy disk was assumed for 4Pi. The profiles (b, d, f) show the OTF-amplitudes along the dashed lines in (a, c, e). To make weak amplitudes in the OTF of I⁵M (e) more visible, (g) shows the same OTF with the colour table normalized to 10% of the maximum value of the OTF. The dashed profile in the inset of (f) corresponds to the experimentally realized case.

data set volume. Deliberately decreasing this size (below the used $\sim 9.6 \mu\text{m}$) increases the minima.

2.2 The I⁵M/4Pi hybrid microscope

Hitherto, 4Pi microscopy and I⁵M have been compared only theoretically^{32,33,26}. To enable a reasonably fair comparison between of the two imaging modes for the same object under equivalent optical conditions, I customized a 4Pi-microscope (TCS 4Pi, Leica Microsystems GmbH, Wetzlar, Germany, **Fig. 2.3**)⁴ with the ability to easily switch between I⁵M and 4Pi mode. The TCS 4Pi is based on a standard confocal beam-scanning microscope but features a 4Pi unit that replaces the objective turret of the standard microscope stand. Since biological imaging is moving from the imaging of fixed cells towards live cell imaging at a fast pace, I decided to compare the performance of the two strongly related concepts for the important case of imaging aqueous samples. To this end, the 4Pi-unit was furnished with two water-immersion objective lenses (PL APO 63x/1.20 W CORR, Leica). The upper lens was a dipping lens allowing the use of a single cover slip to hold the sample and thereby convenient handling, since mounting of the samples between two cover slips was neither required for 4Pi- nor for I⁵M imaging.

In the 4Pi-mode, the radiation from a Ti:Sapphire laser (Mira, Coherent, Palo Alto, CA) is coupled into the confocal scanning unit and is directed into the 4Pi-module, where it is split into two illumination beams by a 50:50 beam splitter cube. The former pupil plane of the microscope turret is transferred into the pupil planes of the two opposing objective lenses by a telescope (**Fig. 2.3** $L_1 - L_2$ and $L_1 - L_3$). Both lenses focus the laser light into the common focal plane. In analogy to the excitation light, the fluorescence collected by the two objective lenses is combined at the beam splitter cube and directed to the detection pinhole of the confocal microscope. A photon-counting avalanche photodiode (APD) connected to the extension port of the microscope's confocal scanning unit enables efficient detection of low signal levels. A bandpass filter (D515/30m, Chroma Technology, Rockingham, VT) was placed in front of the APD. Scanning in the focal plane is performed by the galvanometric mirrors of the scanning unit. For axial scanning, two coupled piezo-electrical actuators move the sample stage up and down.

For I⁵M imaging, the excitation of the sample was performed in the Köhler-illumination mode using the microscope's widefield 100 W mercury-lamp. The fluorescence emerging from the common focal plane of both objective lenses was imaged onto the CCD camera attached to the camera port. The microscope stand can easily be switched between the confocal mode used for

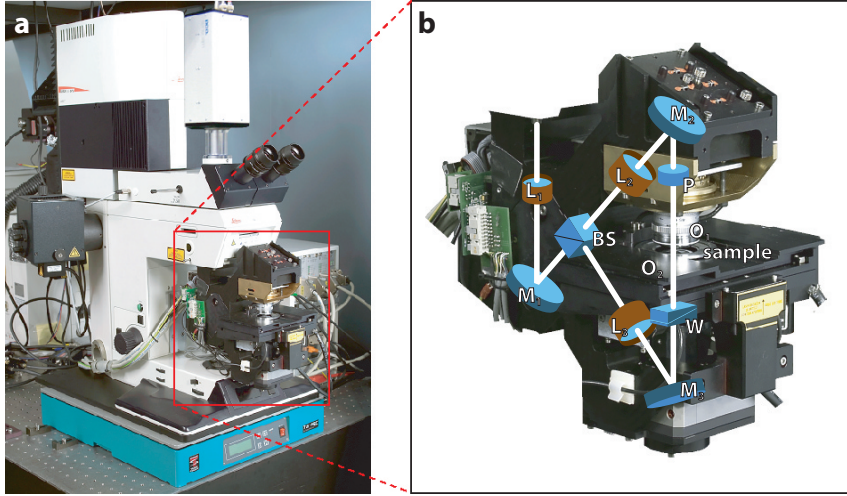


Figure 2.3: Experimental setup for I^5M and $4Pi$ microscopy. (a) The $I^5M/4Pi$ -hybrid microscopes consists of a confocal laser scanning microscope and a interference module (red frame) that supports the two opposing objective lenses. (b) The sample is illuminated by the two objective lenses O_1 and O_2 via the lenses L_1 - L_3 , the beam splitter BS and the mirrors M_1 - M_3 . Fluorescence is detected on the same way back. For optimal interference, the dispersion in the two cavity arms can be balanced by the glass wedge pair W and the corresponding glass plate P . For I^5M , a CCD-camera was added to the camera port of the microscope.

4Pi-imaging and the widefield mode that was taken for I⁵M recordings. In the I⁵M-experiments, a standard filter cube with an excitation band of 450-490 nm and detection above 520 nm (Leica filter cube I3) was used. To allow synchronization with the camera readout, the electronics of the sample stage was modified. No polarizer or slit aperture was used in the beam path of the lamp.

The CCD-camera (sensicam qe, PCO AG, Kehlheim, Germany) featured a quantum efficiency of 62 % at 500 nm. The 2/3" CCD-chip has 1376×1040 pixels of size 6.45×6.45 μm^2 . Projected into the sample, this corresponded to a 64×64 nm^2 pixel size and a field of view of 88×67 μm^2 . The readout noise was $\sim 5 \text{ e}^-$ per pixel at a read out rate of 10 frames per second. For further reduction of the background, an additional bandpass filter (Chroma D525/50m) has been used.

To operate at its theoretical limits, I⁵M imaging ideally requires a polarizer producing azimuthally polarized illumination of the lens⁵. Unfortunately, an azimuthal polarizer with an extinction ratio that is large enough to satisfy the conditions of the ideal scalar theory described by equations (2.9) and (2.10) could not be found. Therefore, the objective lenses were illuminated with random polarization and a homogeneous intensity distribution in the pupil plane. This allows the direct comparison of the experimental results with a theory that assumes the angular intensity distribution of an aplanatic system. To evaluate the potential improvement in I⁵M imaging by ideal azimuthal polarization and homogeneous angular intensity distribution, this idealized case was also simulated computationally.

Dispersion correction.

Both I⁵M and 4Pi-C require coherence and a constant phase between the fluorescence light that is detected via each arm of the interference cavity. Since the detected fluorescence covers a rather large part of the spectrum, the cavity has to be designed such that constructive interference at the focal center is obtained for all wavelengths involved. This would be a trivial case if both cavity arms would be exact copies of each other. However, since the thickness of an optical lens is the most costly parameter to be stringently specified, the tolerances of commercially available lenses are typically in the range of tenths of millimeters. Given the fact that modern objective lenses are complex systems of many lenses that are made of different types of glass, two cavity arms that are constructed from similar parts exhibit significantly different dispersion characteristics.

At a wavelength of λ , the total optical path difference $OPD(\lambda)$ between both interferometer arms is given as the sum over the individual OPDs of all

types of material involved:

$$OPD(\lambda) = \sum_i n_i(\lambda) \cdot d_i, \quad (2.11)$$

with $n_i(\lambda)$ being the wavelength dependent refractive index and d_i the difference in path length in material i . This translates into a wavelength dependent phase

$$\Phi(\lambda) = \frac{2\pi}{\lambda} OPD(\lambda) \quad (2.12)$$

and ultimately into a focal intensity

$$F(\lambda) = 1 + \cos \Phi(\lambda), \quad (2.13)$$

which runs between 0 (destructive interference) and 2 (constructive interference, intensity doubled with respect to a single-lens setup). Without dispersion correction, $F(\lambda)$ strongly oscillates (**Fig. 2.4a**). In order to be able to control $F(\lambda)$, correction elements are added to the beampath. In the microscope used for this study, these elements were a pair of wedges and an optical flat (**Fig. 2.3 W, P**), all made of typical optical borosilicate crown glass (BK7, Schott, Mainz, Germany). The wedge pair and flat were mounted in opposite cavity arms so that in a neutral setting the same amount of glass was added to each arm. By shifting a single wedge, this balance could be intentionally disturbed, which in turn introduces an additional term in (2.11) and thereby brings $F(\lambda)$ close to 2 over the whole spectrum used for the excitation and detection (**Fig. 2.4b**).

2.2.1 PSF-measurements

To investigate the performance of the microscope, fluorescent beads (**App. A**) with an emission at around 515 nm were recorded in the 4Pi as well as in the I⁵M-mode. In the 1PE and 2PE 4Pi-modes, 3D stacks of 40 nm diameter beads were imaged following excitation at 488 nm (1PE, Ar-ion laser) and at 870 nm (2PE, Ti:Sapphire laser) respectively. The pinhole was set to 0.9 times the diameter of the Airy disc calculated for 515 nm. The fluorescence was detected with a counting avalanche photodiode (APD). In the I⁵M-mode, 3D data sets of 100 nm diameter beads were recorded by exciting at about 480 nm. Likewise, theoretical PSFs were calculated for all three modes according to the theory described above. A semi-aperture angle of 1.12 rad was assumed corresponding to the 1.2 numerical aperture (NA) of the employed water immersion lenses. The excitation wavelengths were selected as in the experiment. For detection, a fluorescence wavelength of 510 nm was assumed. For 4Pi-imaging, a pinhole

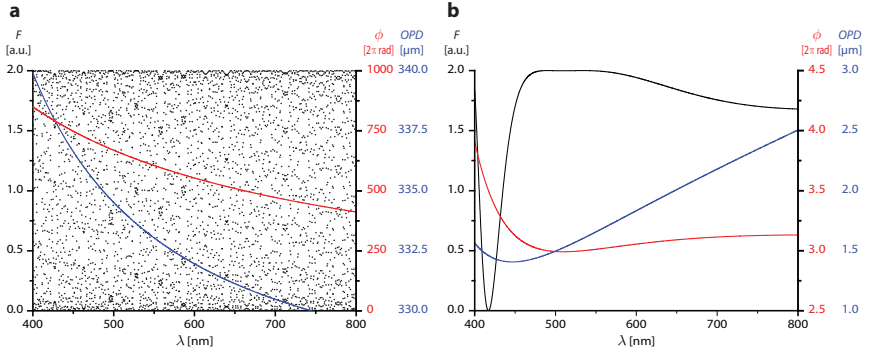


Figure 2.4: Progression of $F(\lambda)$ for 4Pi of Type C and I⁵M. Total optical path difference OPD , absolute phase Φ and focal intensity F over wavelength λ as calculated for typical sets of mismatch in material thickness (BK7- and SF6-glass, air) between both arms of the I⁵M/4Pi interferometer. In this model, the SF6 term is assumed to be unknown and therefore inaccessible for direct compensation. **(a)** Without dispersion correction (+100 μm BK7, +100 μm SF6, +0 μm air), $F(\lambda)$ oscillates strongly. While the excitation phase is still well defined because of narrow bandwidth of the laserline, detection is (quasi-) incoherent, as the manifold interference patterns within any detection window average out. **(b)** Dispersion correction set for optimal interference. Additional BK7 and air terms, introduced by moving W and M_3 (**Fig. 2.3**), yield near-constant $F = 2$ over a broad plateau; (-465 μm BK7, +100 μm SF6, +526.2 μm air). An OPD well below the coherence length of the fluorescence enables coherent detection.

size corresponding to one Airy disc was chosen. The results were in excellent agreement with the theoretical predictions (**Fig. 2.5**).

2.2.2 Comparative imaging of biological specimen.

As a biological test sample, live *Escherichia coli* were treated with Oregon Green as described in methods (**App. A**) to stain the cell walls. This yielded very bright samples, composed of hollow rod-like structures with a diameter of ~ 800 nm. The similarity of the individual bacteria greatly facilitates this study, because it enables a direct comparison of the imaging capabilities even if different bacteria are recorded. x - z -sections were recorded in 2PE 4Pi and in I⁵M-mode (**Fig. 2.6**.)

The 4Pi-data was scanned in x - z -slices with the z -axis being the slow axis. Thus every slice contained the z -profile which is the most sensitive measure for the PSF quality. The adjustment of the system can thus be monitored whilst recording. Eight scans of 256×256 pixels (bi-directional scan mode, 4-times line average) with a pixel size of 73×15 nm² ($x \times z$) were averaged for each slice. The distance between subsequent slices was 97 nm. Typically, 50 x - z -slices had to be recorded to obtain a whole 3D-stack of an *E. coli* bacterium, resulting in a total data acquisition time of ~ 750 s.

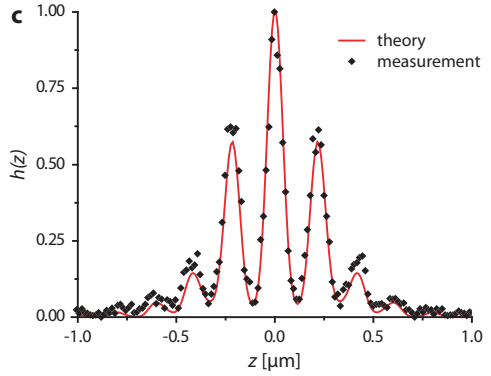
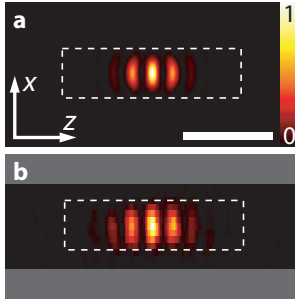
Using a CCD-camera, the I⁵M collects the data as x - y -slices. Our 1376×1040 pixel CCD-chip imaged a sample area of 88×67 μm^2 of which typically a sub-area of 23×21 μm^2 was read out. Each slice was illuminated for 1 s; the axial distance between subsequent slices was 35 nm. Even though the *E. coli* are only ~ 800 nm in diameter, 100 slices had to be recorded to obtain a useful 3D-stack given the axial extent of the I⁵M-PSF. Still, with a recording time of ~ 100 s, the I⁵M-raw data acquisition took 7-8 times less than in the 2PE 4Pi-mode. Moreover, due to the large field of view, a larger number of *E. coli* could be imaged simultaneously.

Recording x - y -planes rather than x - z -sections, I⁵M imaging does not allow the online observation of the z -profile and hence of the phase of the PSF. In order to be able to observe the phase difference at the focal plane, beads were attached to the cover slip. These beads were also used to adjust the microscope after inserting a new sample and to slightly realign the system between two measurements. Beads recorded simultaneously with the bacteria allowed the inspection of the PSF directly from the recorded 3D-stack.

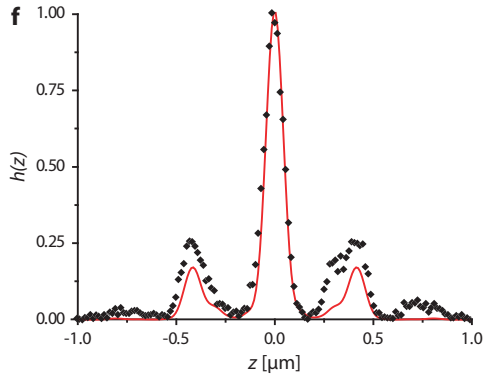
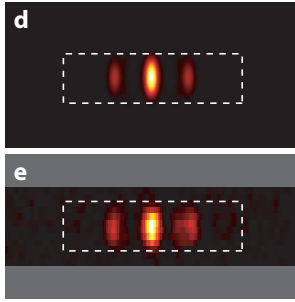
The illumination intensity and the pixel dwell times were chosen in such a way that the dye was bleached by $\sim 1/3$ after recording of a whole 3D-stack. For a thorough comparison, the background in the I⁵M-data was subtracted. The stacks recorded with different imaging modes were resampled to obtain approximately the same pixel sizes for further data processing, i.e. $64 \times 64 \times 17$ nm³

2 A spherical nanosized focal spot unravels the interior of cells

1PE 4Pi Type C



2PE 4Pi Type C



I⁵M

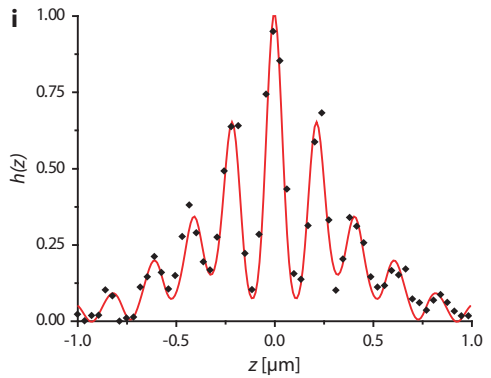
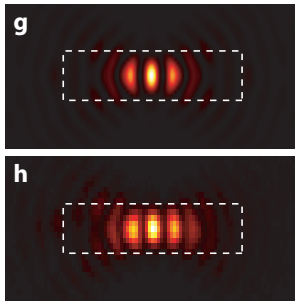


Figure 2.5: Experimental and theoretical PSFs of 4Pi microscopy and I⁵M. Calculated PSFs for (a) 1PE 4Pi Type C, (d) 2PE 4Pi Type C and (g) I⁵M. (b,e,h) x-z-slices of fluorescent beads representing the experimental PSFs of these imaging modes. (c,f,i) z-Profiles of the data, averaged over x as indicated by the dashed boxes. The corresponding z-responses (not shown), given by the lateral x-y-integral of the PSFs, feature slightly higher sidelobes and in I⁵M, they result in a larger background signal of about half of the maximum. Note the good agreement between theory and experiment. Scale bar, 1 μm .

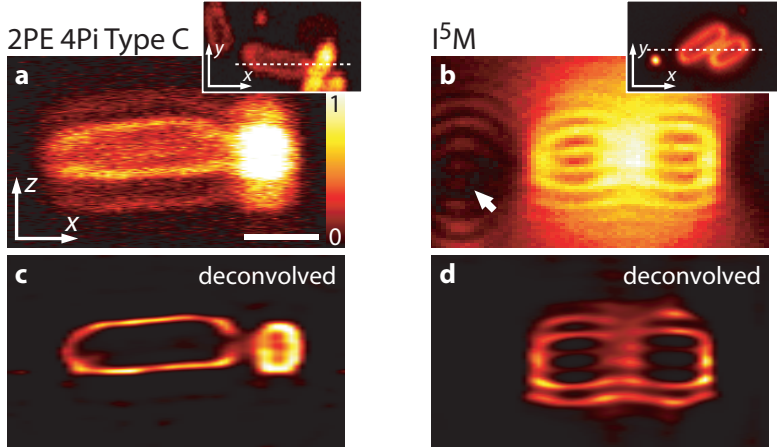


Figure 2.6: Recordings of *E. coli* in 4Pi- and I^5M -mode. Axial (x - z -) slices of *E. coli* stained with Oregon Green. (a) A typical section through a 3D-stack recorded in 2PE 4Pi Type C mode. The color table is normalized to 30 counts to emphasize the darker bacterium out of the two bacteria imaged; the image of the brighter one is saturated. The insets show lateral overviews of the imaged bacteria with the particular positions of the respective x - z -sections marked by the dashed lines. (b) The nonlinearly deconvolved image of the data set (a). (c,d) x - z -slices of the corresponding I^5M -recording. The image (c) is already corrected for bleaching with the color table normalized to 467 counts. The concentric structures (c, arrow) originate from the bead positioned left of the two bacteria and slightly offset from the x - z -slice (see inset). They vividly demonstrate that, contrary to the PSF of 2PE 4Pi Type C, the I^5M -PSF is not separable into a product of one-dimensional functions. Thus objects from adjacent x - z -planes mingle with features from the x - z -plane investigated, making the removal of ghosting more challenging.

and $73 \times 49 \times 15 \text{ nm}^3$ for I⁵M and 4Pi, respectively. With the resampled pixel sizes, signal levels of typically 40 counts/pixel (2PE 4Pi Type C mode) and 400 counts/pixel (I⁵M-mode) were obtained in the regions of maximum signal. The 10-fold larger signal in the I⁵M is due to the more efficient fluorescence generation in 1PE, but also due to the contribution of blurred fluorescence from out-of-focus planes that is collected as well. The latter stems from the fact that I⁵M is neither confocalized nor does it use multiphoton excitation to confine the excitation volume. The blurred signal accumulates in the recorded image, mainly increasing the zero-frequency component in the OTF. Since it adds little to the weakly transferred higher frequencies, this additional signal is rather obstructive to the sidelobe removal by deconvolution.

The recorded data was deconvolved using an iterative positivity-constrained nonlinear Richardson-Lucy algorithm^{39,33} with an optimized set of parameters, with input PSFs obtained from beads recorded either directly before or after the E. coli recording or from beads contained in the same data stack (**Fig. 2.6b,d**). While the deconvolution process removed most of the out-of-focus signal, it was not able to remove the ghosting in the I⁵M-data satisfactorily (**Fig. 2.6d**). An alternative linear approach, Wiener filtering, also failed to provide artefact-free images. The SNR at the weakly transferred spatial frequencies of the I⁵M-OTF was not large enough to raise the signal significantly above the noise background.

2.2.3 Simulations

To rule out differences in the experimental conditions or in the observed structures as potential reasons for the observed disparity in imaging performance, I deconvolved simulated data for the different imaging modes. For the same reason, I also evaluated the potential enhancement of I⁵M-imaging brought about by azimuthal polarization and uniform angular intensity distribution.

To allow a comparison of the performance of the setup with theory, a test structure was tailored to resemble the imaged objects (**Fig. 2.7a,b**). Three hollow E. coli bacteria, two laterally oriented ones that are mutually perpendicular, and a 3-times dimmer one, that is tilted and lying partly on top of the others were modelled with a diameter of 850 nm and a length ranging between $1.8 \text{ }\mu\text{m}$ and $3.8 \text{ }\mu\text{m}$. An additional test structure was included for controlling the achievable quality of the restoration. The test structure consisted of two very thin rods meeting at one end. One of them was oriented in the lateral plane; the other one was eight times dimmer and was also tilted by an angle of 23° with respect to the optical axis. A separate point-like structure was used to indicate the performance of the deconvolution. A pixel size of $60 \times 60 \times 20 \text{ nm}^3$ ($x \times y \times z$) was assumed in order to emulate the experimental imaging condi-

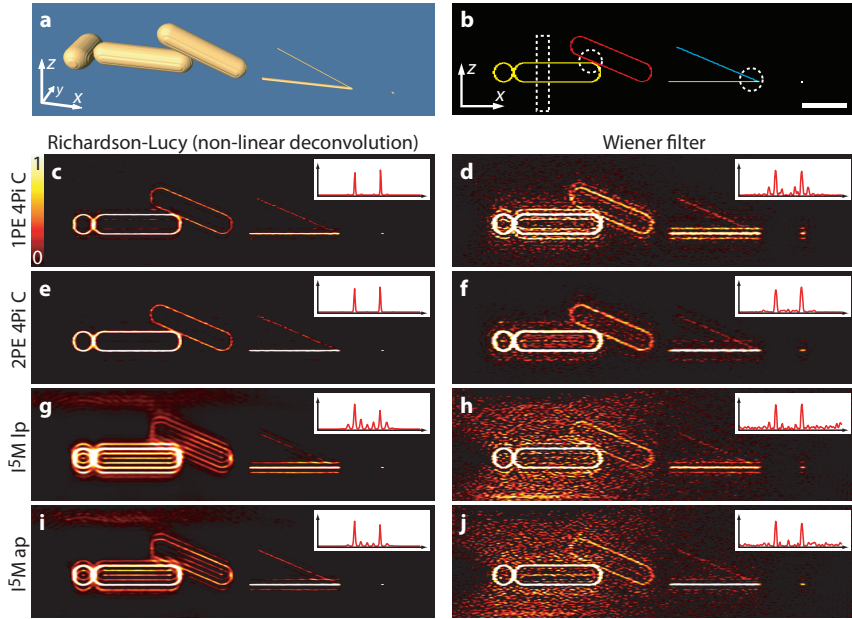


Figure 2.7: Removal of ghosting for different imaging modes. (a) Rendered 3D test structures featuring three 'bacteria', two rods, and a point object. (b) x-z-slice through the test structures. The relative intensities of the red/blue/point structure with respect to the yellow structure are $\frac{1}{3}/\frac{1}{8}/5$. The test structure was convolved with calculated PSFs, normalized to the signal levels that were observed in previous experiments and deconvolved by a non-linear Richardson-Lucy algorithm (left column) or by Wiener-filtering (right column). (c,d) The final images after deconvolution for 1PE 4Pi at a signal level of 120 counts at maximum. (e,f) The 2PE 4Pi data normalized to 40 counts at maximum. (g,h) I^5M data with linearly polarized (lp) illumination similar to the experiment, normalized to 400 counts at maximum. (i,j) The ideal case for I^5M as obtained by azimuthally polarized (ap) illumination with a uniform angular distribution over the complete aperture angle (see main text). To enhance darker regions of the data, the color tables of the deconvolved data sets are normalized to the maximum values of the darker bacterium. This however also enhances the remaining ghosting of the brighter structures. The insets represent the z-profiles of the data averaged in the x-direction as indicated by the dashed box in (b). The dashed circles in (b) point out regions where artefacts arise most likely in the deconvolution process. Scale bar, 2 μm .

tions. To minimize deconvolution artefacts at the boundary of the data stack, a border of about $1.5\ \mu\text{m}$ was added at all sides of the combined structure, resulting in a data stack size of $18 \times 5 \times 5\ \mu\text{m}^3$ ($x \times y \times z$).

This test object was convolved with the appropriate theoretical PSFs (**Fig. 2.2**). To avoid convolution artefacts from periodic boundary conditions, all data stacks and PSFs were calculated for a larger volume and subsequently cut to the final size after convolution. For I⁵M, two sets of conditions were calculated: i) unpolarized excitation as in the experiment and ii) azimuthally polarized light with a uniform pupil function that increases the OTF-minima slightly (**Fig. 2.2f**, inset). As the signal strength is an important parameter for proper simulation, it was hence derived from the experimental data. In order to assess their faithfulness, the images obtained after restoration could also be directly compared with the original structure. In the maxima of the horizontally aligned bacteria, 40 counts per pixel, 120 counts per pixel and 400 counts per pixel were assumed for 2PE 4Pi, 1PE 4Pi and I⁵M, respectively. Subsequently, Poisson statistics was applied to this signal. Background was omitted that typically adds to the I⁵M-data due to readout noise and the missing confocal suppression of out-of-focus light originating from regions outside the recording volume. In general, a perfect I⁵M imaging system was assumed.

To assess the information content of the simulated raw data of the microscope, Richardson-Lucy restoration (**Fig. 2.7c,e,g,i**) and Wiener filtering (**Fig. 2.7d,f,h,j**) were applied as described earlier in the experimental section. The regularization parameters and the number of iterations were chosen such that the apparent differences between the results obtained by deconvolution and the original structure were minimal. To draw attention to the faint structures in the simulated data set, the colour table is normalized to the maximum of the deconvolved signal of the dimmer bacterium. Consequently, the colour table saturates at higher signal levels, which also enhances the visibility of the residual sidelobes of the bright bacteria and the horizontal rod. To give a more quantitative impression of the performance of the deconvolution, the relative sidelobe height after deconvolution is displayed in the insets showing the averaged axial profiles in the region marked by the rectangle (**Fig. 2.7b**). The circles (**Fig. 2.7b**) indicate areas where deconvolution artefacts arise most easily. While for 2PE 4Pi microscopy all structures in the dataset can be reconstructed in essence without producing artefacts, distinct artefacts remain in all I⁵M simulations. This holds despite the fact that the signal is significantly stronger ($\sim 10\times$) in I⁵M. Moreover, the attempt to reconstruct the data makes the weak structures disappear in the proximity of brighter objects. The 1PE 4Pi-confocal mode features moderate ghosting that can be removed with acceptable artefacts, but the 2PE 4Pi-mode is clearly the most favourable.

To further understand the disparity in performance of the two systems, the

Fourier transform of the simulated recordings in the region of the E. coli bacteria for the azimuthally polarized case of I⁵M and for 2PE 4Pi was examined. The region delimited by the positions of the minima of the 4Pi-OTF and the I⁵M-OTF was defined as the critical range of axial spatial frequencies. A closer look revealed that the overall signal-to-noise ratio (SNR) in this region was about three times lower for the I⁵M than for the 2PE 4Pi imaging mode. By examining the Fourier-transformed original structure, it was found that this factor was not due to the object structure being composed of spatial frequencies that are unfavourable for I⁵M. The reason rather was the weak transfer of a range of critical frequencies in this imaging mode. Since this investigation was based on specific samples and limited to one type of objective lenses, the question arises as to what extent the variation of these conditions could possibly improve the I⁵M-recordings, and shall be addressed in the next section.

2.3 Pushing the limits of 4Pi microscopy and I⁵M

Both the 4Pi-OTF and the I⁵M-OTF feature an up to 5-7 fold enlarged support of transferred spatial frequencies in the axial direction as compared to standard microscopy. However, whether this strong increase in axial bandwidth can be transferred into an unambiguous increase in axial resolution depends on the detailed structure of the OTF and the SNR of the data. Low amplitudes in the OTF attenuate the corresponding object frequencies in the image. Offering no true optical sectioning, the I⁵M-OTF features a singularity at the OTF origin. Image reconstruction algorithms increase the signal in the weak frequency regions, but at the same time they also amplify the respective noise. For frequencies with a small SNR, the reconstruction becomes difficult or even impossible and artefacts arise as a result. Solutions to this problem are either to avoid pronounced minima in the OTF or to increase the overall SNR in the image data. By using 2PE and usually also confocal detection, 4Pi microscopy primarily embarks on the first strategy. In contrast, I⁵M relies on a larger signal. To understand how far these concepts can carry, it is essential to take a closer look at the vital elements of a microscope; the sample itself and the objective lenses used.

2.3.1 Objective lenses

The shapes of PSF and OTF are governed primarily by the semi-aperture angle α of the objective lenses used, while distances scale with the reciprocal refractive index of the sample. A larger α yields a PSF with lower sidelobes and better transmission of critical frequencies (**Fig. 2.8.**) The preconditions are that the

field correction of the lenses is adequate in the field of view, and that the large angle focusing conditions are not spoiled by aberrations; note that spherical aberration scales with the fourth power⁴⁰ of α .

Currently, 1.20 NA water immersion lenses are the lenses with the largest semiaperture angle ($\alpha = 64^\circ$) available for live cell imaging. Glycerol and oil immersion lenses with larger α exist, and are a means to boost the capabilities of both I⁵M and 4Pi where imaging in aqueous samples is not required. Since these lenses are designed for embedding media with refractive indices much higher than that of water, aberration-free imaging of watery samples is constricted to the vicinity of the coverslip. As the focal plane is moved further into the sample, aberrations due to refractive index mismatch appear, their strength scaling with the depth⁴¹. Although this is often acceptable in a standard confocal (one-lens) setup, as it will primarily decrease SNR and only slightly lower lateral resolution at first, these are unfavorable conditions for a 4Pi/I⁵M setup. These techniques rely on a diffraction limited focal spot of both lenses for excitation and/or detection to obtain sufficiently low sidelobes, and generally at least one lens will focus deep into the sample. However, imaging of non-live samples allows the use of embedding media different from water, with refractive indices that are tailored to match the design specifications of the respective lens (see **App. A**). A sample that is prepared in this manner does not introduce aberrations at any depth, allowing to tap the full potential of high- α lenses.

The largest semi-aperture angle ($\alpha = 74^\circ$) is provided by oil immersion lenses that have become commercially available for use in total internal reflection microscopy. Combined with two-photon excitation, these lenses finally enable ghost-free 4Pi-imaging of Type C⁴². Furthermore, they enable 4Pi Type A imaging with linear (one-photon) excitation⁴³ and its inherent advantages; a signal that is far stronger than in the multi-photon case, as well as the reduced complexity of Type A detection with regard to Type C (**Fig. 2.4**). These or similar lenses will also improve I⁵M. Given a sample volume of $(10\mu\text{m})^3$, azimuthally polarised light, and aberration-free focusing with $\alpha = 74^\circ$, the minima of the OTF are expected to be up to 1.2%, corresponding to a doubling of the weakly transferred frequencies as compared to the water-immersion lenses used in this study. Nonetheless, I⁵M still suffers from the gap at low frequencies in its OTF, that can be tightened, but not sufficiently lifted.

2.3.2 Sample thickness and recording volume

Compared to many other biological specimens, *E. coli* bacteria are rather thin. For thicker samples, the SNR becomes even worse at the critical spatial frequencies of I⁵M. Unlike in a (4Pi-) confocal or multiphoton excitation setup, unwanted signal from out-of-focus planes accumulates on the CCD-chip. For

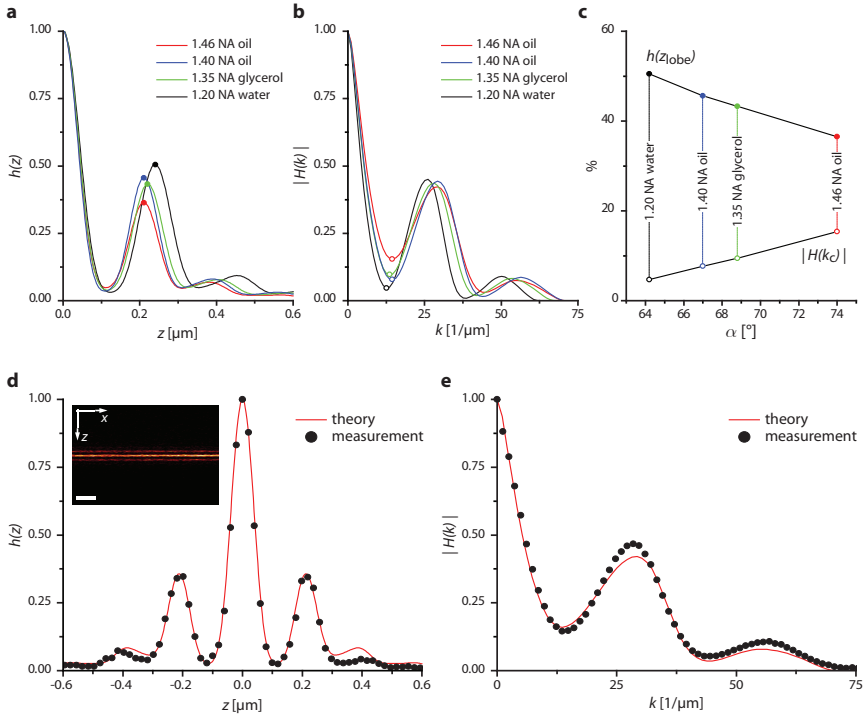


Figure 2.8: Imaging properties of high-NA objective lenses in a 4Pi setup. (a) Calculated z-response $h(z)$ and (b) amplitude $|H(k)|$ of the axial OTF profile for typical objective lenses as a measure of their capability to distinguish between infinitely extended planes that are oriented perpendicular to the optic axis. (c) Height of sidelobes in z-response $h(z_{\text{lobe}})$ (filled circles) and OTF amplitude at corresponding critical frequencies k_c (hollow circles), plotted versus semiaperture angle α . The use of 1.46 NA oil immersion lenses yields an 28% reduction in sidelobe height, equal to about 230% gain in transmission of critical frequencies over 1.2 NA water immersion lenses. (d) Experimental z-response of 1.46 NA oil immersion lenses (HCX PL APO 100x/1.46 OIL CORR, Leica Microsystems, Germany), as measured with an Nk51 dye layer (inset: raw data, scale bar 1 μm) in real and (e) reciprocal space. Parameters for calculations and experiment; single-photon excitation at $\lambda_e = 514$ nm, Type C detection centered at $\lambda_d = 565$ nm, pinhole size 0.5 AU (a-c), 0.7 AU (d,e).

planes that are a few microns away from the focal plane, this background is so blurred and featureless that it adds only to the lower frequencies that are close to the OTF origin; the contributions to the critical frequencies remain rather low. Consequently, although the recorded data appears much brighter, this additional signal does not add to the structural information of the object; it mainly is an additional source of noise.

This reasoning also holds for thin samples when increasing the recording volume in the axial direction. For planes far away from the sample, the de-focused fluorescence is still detected. Again, this light lacks large frequency components and only contributes to the OTF origin. Confining the recording volume, on the other hand, complicates the image deconvolution since the signal of the structures of interest is cut off at the image borders. While in 2PE-4Pi microscopy the PSF is axially confined to $\sim 1\ \mu\text{m}$, the extent of the inherently non-confocalized I⁵M-PSF is unlimited. To avoid ringing artefacts in restoration, it is therefore necessary to extend the recording volume well over the imaged structure. For the presented data, $\sim 1.5\ \mu\text{m}$ were appended in each direction. However, no matter whether the sample volume or the recording volume is considered or not, the relative height of the minima of the I⁵M-OTF scales inversely with the axial extent of either volume. This stems from the fact that the latter defines the sampling of the OTF in frequency space, especially of the central singularity representing the total signal. Therefore, large sample volumes correspond to high overall background levels and the OTF minima tend to zero in relation to the background.

Irrespective of the subtleties with regard to the singularity of the I⁵M-OTF, both experiments and calculations show that unlike in 2PE 4Pi microscopy, artefact-free deconvolution of I⁵M images of general samples is currently not possible with water immersion lenses. These findings are based on rather thin samples, meaning that with thicker samples the artefact issue is aggravated. Therefore, an important outcome of this study is that the substantially stronger fluorescence signal of I⁵M cannot compensate for its much weaker transfer of critical frequencies. Nonetheless, contrary to standing wave microscopy^{44,45} which does not provide axial superresolution in 3D-imaging^{46,32,47}, I⁵M features a continuous frequency transfer within its region of support. This important property leaves I⁵M valid as a conceptually viable approach for axial resolution improvement.

This raises the question as to whether special cases exist that lessen the severity of these issues. And indeed, if the axial extension of the sample is less than the distance between lobes of the PSF, i.e. typically about 200 nm, the image components that stem from the main PSF peak and from the sidelobes do not overlap. For sample sizes up to twice this value ($\sim 400\ \text{nm}$), the valid axial imaging region contracts towards the center x-y-plane of the sample.

Image deconvolution within this region can be replaced by a simple clipping operation that restores image content at critical frequencies by providing a priori knowledge about the sample size. While this method of constraining the sample thickness to about four times the available axial resolution might seem of lesser importance, it will become much more attractive as resolution is enhanced further, and attention shifts to smaller structures such as cellular organelles, that naturally satisfy this constraint.

2.4 isoSTED microscopy

Both 4Pi and I⁵M feature are a huge resolution improvement over conventional microscopy, drawing their resolving power from an increased aperture that encompasses a near complete 4π solid angle. Still, the shapes and sizes of the foci they create are governed - and limited - by diffraction. To overcome this fundamental barrier towards nanoscale resolution, the integration of a switching mechanism is a logical step. Both philosophies - the sequential readout in case of the 4Pi, as well as the maximal parallelized readout of the I⁵M - are compatible with this strategy. However, reducing the size of the effective PSF by switching off parts of the sample that would otherwise fluoresce, inevitably comes at the price of a lowered signal. The relative strength of out of focus components in the detected signal will thereby increase and lower the available SNR. Considering this, the missing confocality of I⁵M-excitation that expresses itself in the singularity of the I⁵M-OTF weighs heavier than the prospect of a parallelized readout, and motivates the decision to base further progress on a 4Pi-configuration.

2.4.1 STED augmented 4Pi microscopy

While the inherent modulation of a 4Pi-focus is the source of sidelobes, it also offers a unique way of removing them while simultaneously pushing the axial resolution even further beyond that of a standard confocal microscope: a second incoming beam can be used to generating a second 4Pi-focus that is centered on the excitation focus but tuned to the opposite 4Pi-phase. This beam then switches off unwanted fluorescence away from the their common focal center. For this study, a standard beam scanning confocal microscope (Leica TCS NT) with fast galvanometric beam deflectors (TCS NT, Leica Microsystems GmbH, Wetzlar, Germany) was equipped with a custom made 4Pi unit, and a modified UV port to accept the STED beam(s) being used for switching.

A pulsed STED scheme was employed, where a short excitation pulse at $\lambda_e = 514$ nm was immediately followed by a STED-pulse $\lambda_{\text{STED}} = 647$ nm (STEDz

for axial confinement). Two laser systems generated the pulses, operating at a repetition rate of 72 MHz. A mode-locked mixed gas Argon/Krypton-ion-laser (modified Innova 70 Spectrum, Coherent Inc., Santa Clara, CA, USA) provided the excitation pulse. The STEDz-pulse originated from a second mode-locked mixed gas ion-laser (modified Innova 70C Spectrum, Coherent Inc., Santa Clara, CA, USA). The same HF-oscillator (custom built PulseDrive Dual, APE, Berlin, Germany) drove the mode-locker units of both lasers, with a variable phase between them, thus generated two synchronized pulse trains with an adjustable time delay. The original width of both pulses was 200 ps, which was still a factor of ten smaller than the lifetime of a typical fluorophore (about 2 ns), but already long enough to prevent damage to the sample by nonlinear processes. Unlike with femtosecond modelocked Ti:Sapphire lasers and optical parametric oscillator systems, the need for pulse stretching was therefore eliminated. Excitation and STED light entered the STED-4pi microscope via optical fibers. Temporal alignment was performed by measuring the received fluorescence from a remote part of the sample and adjusting the pulse delay for maximum STED efficiency.

To provide optimal imaging conditions, 4Pi Type C was chosen as imaging mode and dispersion correction elements were installed. To get the excitation and the depletion beam into counter-phase, i.e. $F(\lambda_{\text{STED}}) = 0$, the dispersion correction was tuned to an intermediate state (**Fig. 2.9**). The choice of objective lenses fell in favour of 1.46 NA oil-immersion lenses (HCX PL APO 100 \times 1.46 NA OIL CORR, Leica Microsystems, Wetzlar, Germany). In support of their high aperture angle ($\alpha=74^\circ$), a correction collar on these lenses allows one to compensate small deviations in sample temperature and refractive index that would otherwise aberrate the focus.

The performance of the system was assessed by measuring the z-response of the microscope with a thin NK51 dye layer. The fluorescence was detected over a spectral window of $\lambda_d = 542\text{-}588$ nm. The phases for excitation, depletion and detection in Type C mode, were kept virtually constant over a scanning field of at least 16 μm width (**Fig. 2.10a**). Without STED light applied, the axial FWHM was ~ 90 nm together with a sidelobe height of 39 %. Turning on the STED beam with an average power of 5 mW dropped the respective values to ~ 50 nm and 17 %, yielding a transmission of critical frequencies that rivals 2PE-4Pi-C, as well as the highest far field resolution obtained from a beam scanning microscope at the time of this experiment (**Fig. 2.10b,c**).

The observed drop in peak signal (**Fig. 2.10a**) in STED-4Pi-C mode with respect to 4Pi-C is partly due to a low-intensity 'belt' of STED light around the focus in the focal plane (**Fig. 2.9b**), that slightly enhances lateral resolution while STED power is applied. This effect is small compared to the axial compression of the focal spot, but nevertheless visible as a reduced peak am-

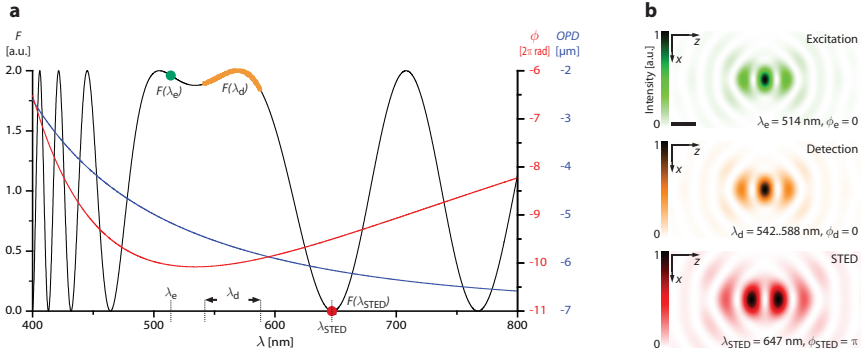


Figure 2.9: Progression of $F(\lambda)$ for STED-4Pi of Type C. Total optical path difference OPD , absolute 4Pi-phase Φ and focal intensity F over wavelength λ as calculated for a typical set of mismatch in material thickness (BK7- and SF6-glass, air) between both arms of the 4Pi cavity. In this model, the SF6 term is assumed to be unknown and therefore inaccessible for direct compensation. (a) STED-4Pi with de-tuned dispersion correction, in order to achieve destructive interference for the depletion beam ($F(\lambda_{STED}) = 0$), while leaving Type C detection intact; (-220 μm BK7, +100 μm SF6, +147.2 μm air). (b) Focal intensity distributions.

plitude of the z -response. However, it only accounts for about half of the loss observed. The other half can be attributed to a low amount of STED intensity at the focal center, arising from slight aberrations introduced by residual imperfections in the beam path.

2.4.2 Spherical focal spot generation

The STED-4Pi microscope proved that molecular switching can be used to great success in a 4Pi-configuration, and that the technical challenges can be met. However, as resolution increases, so does the requirement for stability of the microscope. This was accounted for by the development of a new 4Pi-module (**Fig. 2.12**), that offered enhanced accessibility and thermal stability. Furthermore, the new microscope was designed to work in 4Pi Type A mode, as STED now supersedes Type C detection for providing sidelobe suppression and deepened PSF modulation.

The previous set of lasers was upgraded to a total of four linked laser systems that kept operating at a repetition rate of 72 MHz. The excitation light was now provided by one of two alternative semiconductor lasers (PicoTA 490 and PicoTA 530, pulse width < 100 ps, PicoQuant, Berlin, Germany). A small fraction of every STED-pulse was coupled out to a fast photodiode to trigger

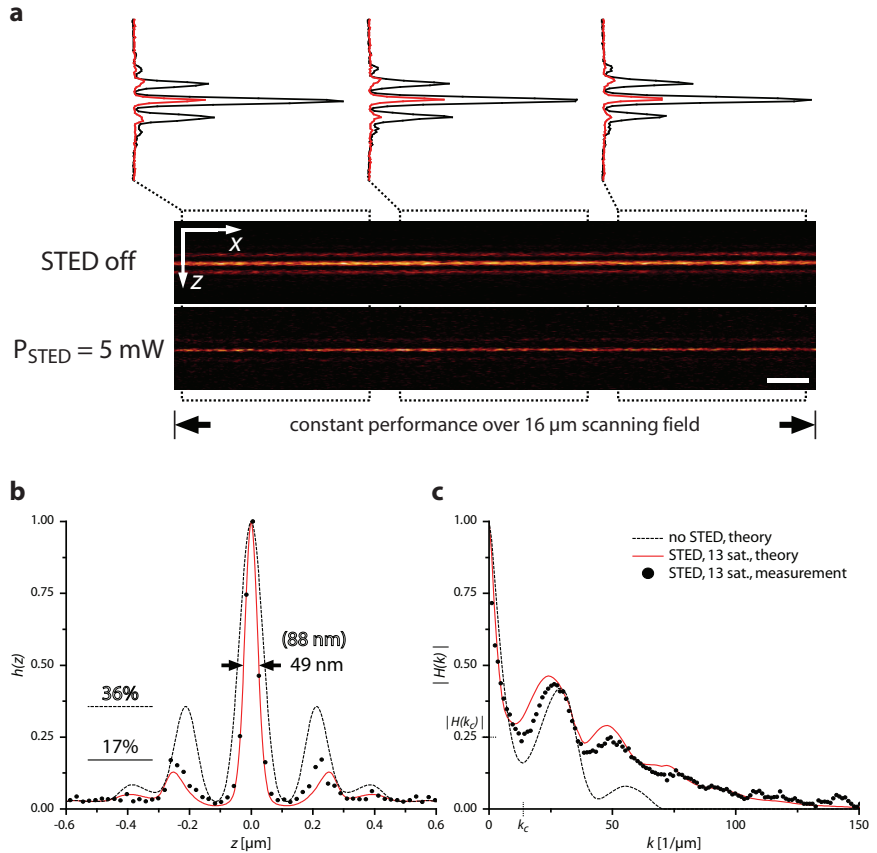


Figure 2.10: Performance of the STED-4Pi beam scanning microscope. (a) x-z-section of a thin fluorescent NK51 layer (A). Images depict raw data; a measurement in STED augmented 1PE-4Pi-C mode compared to a reference scan with no applied STED power. Profiles over the left, center and right region of the $16 \mu\text{m}$ scanning field reveal near-constant 4Pi phases. (b) Properties of the experimental z-response. STED augmentation at a power of $P_{\text{STED}} = 5 \text{ mW}$, corresponding to a maximum intensity of 13 saturation intensities around the focal center, yields an axial FWHM of 49 nm and suppresses sidelobes to 17 % of the main maximum. (c) The amplitude $|H(k_c)|$ of the respective axial OTF profile at critical k_c is thereby raised to $\sim 25 \%$ of the main peak, a value at which image restoration is usually attained easily. Scale bar $1 \mu\text{m}$.

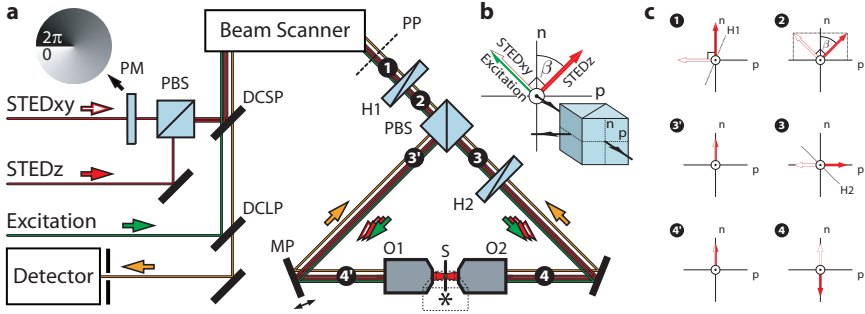


Figure 2.11: Fluorescence microscopy setup with isotropic 3D focal spot. (a) Beams for excitation, STEDxy (lateral) and STEDz (axial) are combined using a dichroic mirror (DCSP) and then fed through a beam scanner into a 4Pi unit with two opposing objective lenses (O1 and O2; HCX PL APO 100 \times , 1.46 NA OIL CORR; Leica Microsystems). The fluorescence light collected by both lenses backpropagates along the same optical path to the detector, passing through the DCSP and a second dichroic mirror (DCLP). The pivot plane (PP) of all scanning beams is conjugated to the entrance pupils of the objective lenses. The incoming beams are divided by a polarizing beam-splitter (PBS) and coherently superimposed at both lenses' common focal plane inside the sample (S). A piezodriven mirror (MP) controls the difference in pathlength between both cavity arms and thereby the 4Pi phases of all beams. The polarization state of STEDxy and STEDz is adjusted by two half-wave retarder plates (H1 and H2). Numbers in black circles indicate points for which these polarization states are displayed in c. *, see 2.13 for focal intensity distributions. (b) The excitation beam and the STED beams for lateral (STEDxy, imprinted with a circular phase ramp (PM)) and axial (STEDz) fluorescent spot compression are polarized under $\beta = 45^\circ$ with respect to the perpendicular direction (n) to the splitting plane (p) of the polarizing beam-splitter. STEDxy and STEDz are polarized orthogonal to each other. (c) Polarization state of STEDxy (outlined) and STEDz (solid) at indicated points in the setup. By tuning the orientation of the half wave retarder plate H1 and thereby β , the branching ratio between both arms is adjusted for matching intensities of the partial beams (position 1 and 2). Right behind the polarizing beam-splitter, the partial beams of STEDxy and STEDz are mutually orthogonally polarized (positions 3 and 3'). Parallel polarization for both beam pairs is rectified by the second half wave retarder plate H2 (positions 4 and 4'). Notably, the relative phase between the STEDxy and STEDz beam pairs now differs by π .

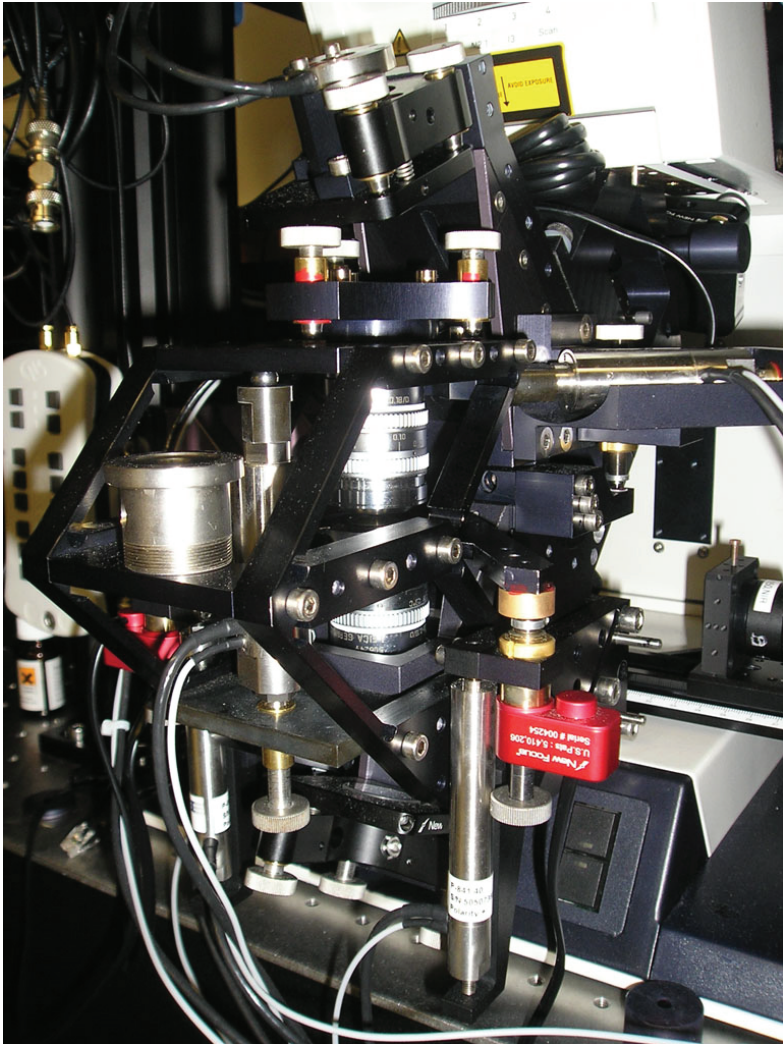


Figure 2.12: 4Pi-module of the isoSTED microscope.

these lasers via a custom built electronic picosecond-delay unit. Temporal alignment was performed by measuring the received fluorescence from a remote part of the sample and adjusting all delays individually for maximum STED efficiency.

Contrary to a standard 4Pi microscope, the counterpropagating beam pairs were produced by a polarizing beam splitter. To still enable coherent field addition in the focal region, the polarization was rectified in one of the arms using a $\lambda/2$ retarder (**Fig. 2.11a**). The use of a polarizing splitter was important in this arrangement because it allowed the amplitudes of the two outgoing partial beams to be matched by tilting the polarization plane of an incident beam by an angle β of about 45° with respect to that of the splitter (**Fig. 2.11b**). Moreover, it enabled synthesizing the STED intensity patterns by the (incoherent) addition of two differently but simultaneously generated light patterns featuring a common focal zero: one for lateral (STEDxy) and one for axial (STEDz) squeezing¹⁰.

To prevent mutual interference, these patterns were produced at the same wavelength, λ_{STED} , but with two different lasers. To meet the increased demand for power, the former excitation laser Innova 70 was replaced by a mode-locked Krypton-ion-laser (modified Innova Sabre, Coherent Inc., Santa Clara, CA, USA) that now provided the additional STEDxy-pulse. Polarization of the two incoherent laser beams was tilted by 45° with respect to that of the beam splitter, but kept orthogonally oriented with respect to each other (**Fig. 2.11b,c**). Before the wavefront of the STEDxy beam entered the triangular cavity, a phase plate imprinted it with a circular phase ramp to render a doughnut shape in the focal region. Constructive interference of the phase-modified partial beams at the focal point doubled the field intensity in the doughnut, which led to a more efficient depletion compared to a single lens setup, while the central zero was left intact. The regularly focused partial waves of the STEDz beam also interfered at the focal point, but due to its orthogonal polarization orientation with respect to its STEDxy counterpart (**Fig. 2.11c**), the partial beams of the STEDz beam interfered destructively, which rendered a central zero with steep edges along the z-axis. Thus, the polarizing beam splitter tightly locked the two patterns to 'orthogonal' interference. The superposition of these focal intensities yielded a focal '3D doughnut' of uniform polarization state that virtually enclosed the geometrical focal point (**Fig. 2.13**).

An optical path length difference was advantageously selected that, besides installing the above pattern for fluorescence inhibition, rendered constructive interference for the excitation light at the excitation wavelength, λ_e . Whereas the axial extent of the main maximum of the PSF was thus reduced by a factor of 3 (compared to a single lens setup) the actual benefit here was that the

2 A spherical nanosized focal spot unravels the interior of cells

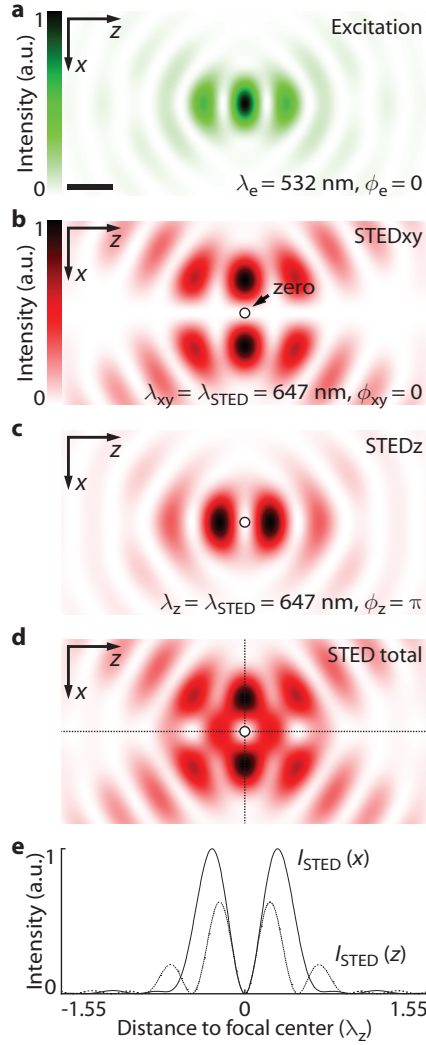


Figure 2.13: Formation of the isoSTED depletion PSF. Calculated focal intensity distributions with respective wavelengths, λ , and 4π phases Φ . **(a)** Constructive ($\Phi_e = 0$) interference pattern of the excitation light. **(b)** Constructive ($\Phi_{xy} = 0$) interference pattern of STEDxy. The doughnut-like shape is generated by a phase mask (PM, 2.11a). **(c)** Destructive ($\Phi_z = \pi$) interference pattern of STEDz. **(d)** Incoherent superposition of both STED beams with relative intensities of 1.0 (STEDxy) and 0.2 (STEDz). **(e)** Focal STED intensity profiles along the x and the z -axis (**d**, dotted lines). The matching intensity gradients enable isotropic compression of the fluorescent spot and hence of the effective PSF of the microscope. Circles mark central points of vanishing field intensities. All calculations were carried out for a 1.4 NA oil immersion lens. Scale bar, 250nm.

excitation focal volume was cut down by half, which reduced the photobleaching by the same factor. Making STED_{xy} about fivefold more intense than STED_z ensured that the intensity profiles, I_{STED} (**Fig. 2.13e**), around the common central zero intensity point were equally steep along x , y and z axes. As a result, the fluorescence spot was isotropically compressed following a square-root law⁴⁸ to a subdiffraction-sized sphere of diameter d :

$$d \approx \lambda / \left(2NA\sqrt{1 + I_m/I_s} \right), \quad (2.14)$$

with NA denoting the numerical aperture of the lens, $I_m = \text{maximum}(I_{\text{STED}}(z))$, and I_s denoting the intensity at which the ability of the fluorophore to emit is cut down by half. I termed this concept isoSTED, because for $I_m > 5I_s$, the fluorescence spot became essentially a sphere with diameter

$$d \approx \lambda / \left(n\pi\sqrt{I_m/I_s} \right), \quad (2.15)$$

where n is the refractive index of the sample. For $I_m/I_s \rightarrow \infty$ and a perfect central zero, the spherical fluorescence spot uniformly converges to a point.

Experimental verification and application.

The calculated effective PSF of a confocal fluorescence microscope at $NA = 1.4$, $\lambda_e = 532$ nm and fluorescence wavelength $\lambda_f = 580$ nm was compared with that of an isoSTED microscope using the same lenses and operating with $\lambda_{\text{STED}} = 647$ nm and $I_m/I_s = 15$ (**Fig. 2.14a**). The isotropic PSF of our system was verified by imaging 21-nm-diameter fluorescent beads (**Fig. 2.14b**). In the normal confocal mode (that is, illumination through a single lens and no STED beam, $NA = 1.46$), the full-width-half-maximum (FWHM) of the focal spot amounted to 165 nm in the lateral and 405 nm in the axial direction. Switching on the isoSTED mode with an average power of (merely) $P_{xy} = 20$ mW for the lateral and $P_z = 3$ mW for the axial STED beam, confined the fluorescence generation mainly to the central zero of the focal STED pattern. In good agreement with the calculation, we obtained a nearly spherical main maximum of the PSF displaying a FWHM of 40, 41 and 44 nm in the x , y and z directions, respectively (**Fig. 2.14c**). The only difference to the calculation was that some signal ($< 35\%$ of the main peak) was also generated at the first-order side-minima along the optical axis, a feature of the PSF that can be readily dealt with by linear or nonlinear deconvolution of the image data. Notwithstanding this, the experimental isoSTED PSF was dominated by a main maximum delivering an isotropic 3D resolution of $\sim \lambda/16$.

Next, the distributions of mitochondrial proteins was investigated in morphologically intact fixed mammalian cells. Mitochondria are spherical- to

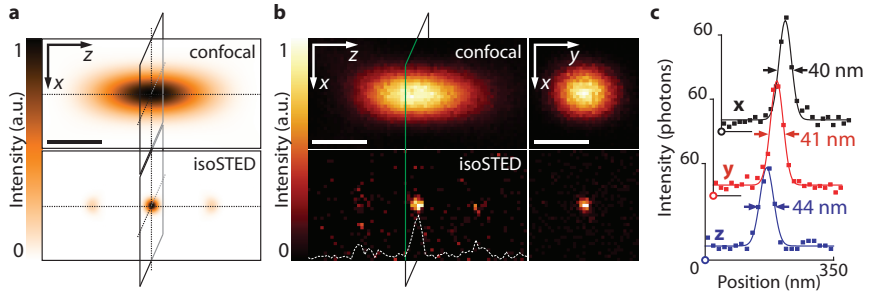


Figure 2.14: Isotropic effective focal spot (PSF) on the nanoscale. (a) Calculated PSF of a confocal fluorescence microscope and the corresponding spherical PSF of the isoSTED microscope at $I_m/I_s = 15$ ($NA = 1.4$; wavelength parameters as in **Fig. 2.13**). (b) Experimental counterpart to **a** as measured with a 21-nm-diameter fluorescence bead. The FWHM of the confocal setup (1.46 NA) is 165 nm in the lateral and 405 nm in the axial direction. Switching on the STED pattern shown in **Figure 2.13d** leads to a largely spherical main focal fluorescence spot. (c) Gaussian fits through the lateral and axial profiles of the focal spot yield indicated FWHM, corresponding to an isotropic far-field optical 3D resolution of $\lambda/16$. Baselines are marked with colored circles. Scale bars, 250 nm.

tubular-shaped organelles with an inner and an outer membrane. So far, the 200-400 nm diameter of this organelle has virtually prevented the visualization of spatial protein distributions in mitochondria by light microscopy. The translocase of the mitochondrial outer membrane (TOM complex) serves as the mitochondrial entry gate for the vast majority of nuclear-encoded protein precursors^{49,50,51}. Acting as a primary import receptor, Tom20 is a subunit of the TOM complex. Biochemical evidence suggests that the TOM-complex is enriched in so-called contact-sites involved in the translocation of proteins. We immunologically labeled Tom20 with the orange-emitting organic fluorophore NK51 (Atto-Tec GmbH, Siegen, Germany). We chose this fluorophore because the laser lines for λ_e and λ_{STED} perfectly match its excitation and emission spectra.

A 3D stack of 62, < 50 nm thin optical sections (x-y images) through a mitochondrion was recorded inside a mammalian (Vero) cell, with a spacing of 22 nm in the z dimension. A maximum likelihood expectation maximization⁵² (EM) method was applied to remove the effect of the sidelobes above and below the main spherical focal spot in the 3D image stack (**Fig. 2.15**). A first estimate of the PSF was obtained from a small subset of the raw data. Subsequently, the whole data set was deconvolved by 15 iterations of a Richardson-Lucy algorithm³⁹. The quality of the PSF estimate was then assessed by measuring the spurious signal outside the organelle. The final data was obtained by

iterative refinement of the PSF estimate with regard to the minimization of this signal.

Individual sections, recorded at the bottom, center and the top of the organelle, revealed that Tom20 forms distinct clusters at the organelle's boundary (**Fig. 2.15a-c**). Since the x - y images are part of a 3D stack, we rendered a 3D representation of the Tom20 distribution (**Fig. 2.15d**). The isotropic resolution was essential to identify the peripheral localization of Tom20. Summing up all x - y images simulated a purely two-dimensional nanoscopic method. The resulting image (**Fig. 2.15d**) revealed that a method lacking axial subdiffraction resolution cannot be used to identify the location of the clusters at the periphery of the organelle.

2.4.3 Dual-color 3D nanoscopy imaging

A second color channel was added to demonstrate the ability of *isoSTED* to image the spatial relationship of two or more biomolecules at the nanoscale in three dimensions. The organic fluorophore DY-485XL (Dyomics GmbH, Jena, Germany) exhibits a similar emission spectrum as NK51 and hence can be quenched by the same $\lambda_{\text{STED}} = 647$ nm. However, as its excitation spectrum is blue-shifted by ~ 50 nm (**Fig. 2.16**), these fluorophores could be discriminated by choosing 488 nm as the excitation wavelength for color channel 1 (DY-485XL) and the customary 532 nm for channel 2 (NK51). This scheme was very attractive because it used the same STED beam zero for both channels, which therefore were inherently aligned with respect to each other.

Two-color images were recorded by consecutive excitation of both channels. Although the excitation wavelengths were separated by more than 40 nm and corresponded well to the respective dye's absorption maximum, the other fluorophore was also slightly excited. This introduced some cross-talk in the data, resulting in pixel counts of channel 1 and channel 2 that were a linear combination of the contributions from both dyes. As the cross-talk could be determined, linear spectral unmixing⁵³ effectively separated the DY-485XL and NK51 fluorescence. The strength of the cross-talk depended on the relative intensities of the excitation lasers and therefore varied slightly for each recording. Therefore, only those sets of images were considered for further analysis that contained enough information to directly determine the unmixing parameters. Most of the recordings contained isolated agglomerations of secondary antibodies. Plotting all pixel values (corresponding to isolated agglomerations) in channel 1-channel 2 space showed that two distinct and well-defined groups could be identified, representing agglomerations consisting of either DY-485XL-conjugated or NK51-conjugated antibodies. The magnitude of the cross-talk was quantified by analyzing both groups. For the data shown in **Fig. 2.16ac**,

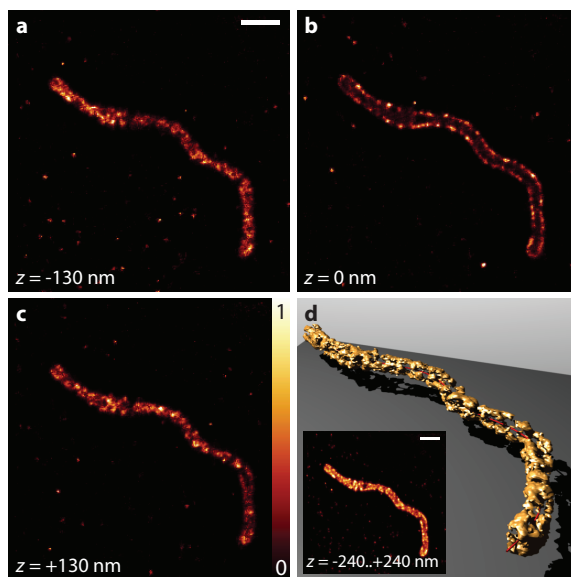


Figure 2.15: isoSTED fluorescence microscopy dissects a mitochondrion. By focusing light into the interior of a mammalian (Vero) cell, isoSTED images the distribution of the protein Tom20. (ac) Optical sections through the bottom (a), center (b) and top (c) planes of the mitochondrion reveal distinct Tom20 clusters. The x - y image through the center plane shows that the clusters are located at the rim of the organelle. The sections shown are part of a 3D stack of 62 x - y images, all equally spaced in the z dimension by 22 nm. The image data shown were obtained after deconvolution as described in Methods. (d) 3D reconstruction of the Tom20 distribution (the red filament is to guide the eye). Inset, sum of all x - y images from $z = -240$ nm to $z = +240$ nm. This mimics a nanoresolving (STED) microscope with standard confocal resolution along the z direction, showing that axial super-resolution is essential for unraveling the protein distribution in this sub-wavelengthsized organelle. Scale bars, 1 μ m.

the ratio between channel 1 and channel 2 was 84:16 for DY-485XL and 23:77 for NK51. The corresponding values for the control (**Fig. 2.16e**) were 86:14 and 25:75.

As a second protein, the matrix protein mtHsp70 (also referred to as mortalin or GRP 75) was investigated, a component of the mitochondrial protein import motor^{49,50,51}. Regulated cycles of mtHsp70 binding to precursor proteins and its subsequent release mediate vectorial movement of the precursor proteins toward the matrix. The intermittent association of mtHsp70 with the import machinery may suggest that a sizeable fraction of the mtHsp70 pool is at any time associated with the inner membrane of the mitochondrion. However, no enrichment of mtHsp70 at the mitochondrial rim was found, indicating that the majority of mtHsp70 is located in the mitochondrial matrix (**Fig. 2.16b**).

The features visible in the individual images of Tom20 (DY-485XL; **Fig. 2.16a**) and mtHsp70 (NK51; **Fig. 2.16b**) in the middle plane of the very same mitochondrion are equivalent to those observed in single-color experiments (**Fig. 2.15**) and therefore indicate that the isotropic resolution is in the 50-nm range for both channels. The details in channel 2 (NK51) appear to be slightly sharper, which is due to a comparatively better STED efficiency of this dye at 647 nm. Reversed labeling of the two proteins served as a control and exhibited essentially the same features (**Fig. 2.16e**). In both cases, the Tom20 protein clearly delineated the mitochondrion. Note that apart from the linear unmixing, the shown data (**Fig. 2.16**) are raw, that is, non-deconvolved. The dual-color images (**Fig. 2.16c,e**) are, to my knowledge, the first light microscopy recordings separating two proteins of an organelle inside a whole cell with nanoscale 3D resolution. This clearly demonstrates the emerging capability of optical microscopy to image the interior of nanosized subcellular organelles with regular lenses and visible light.

2.4.4 **isoSTED microscopy with a single depletion beam**

In order to reduce the complexity of the microscope and to speed up the necessary alignment procedures, a variant of isoSTED microscopy has been developed that relies on a single depletion beam (isoSTED-sdb) for providing the 3D compression of the focal spot. The key concept is to create and exploit a controlled build-up of the axial (z) field component above and below the focal center of the STED_{xy} beam (**Fig. 2.17**). The z -component of the total intensity distribution (**Fig. 2.17g**) can then serve as substitute for the STED_z beam by providing side-maxima suppression and axial compression of the focal spot. Since lateral and axial compression is achieved by means of different field components, the shape of the resulting focal spot depends on the relative depletion efficiency that these components provide. Among

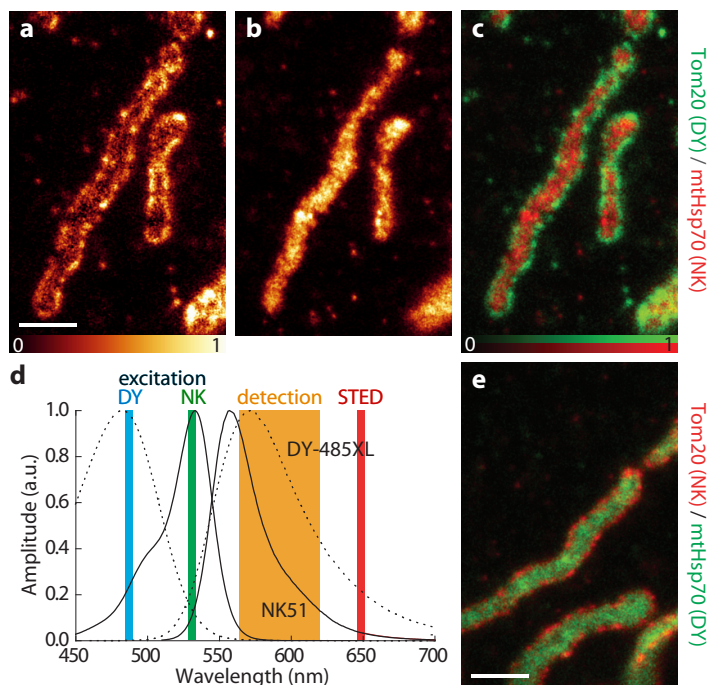


Figure 2.16: Two-color isoSTED imaging of mitochondria in Vero cells. (a,b) Distribution of the outer membrane protein Tom20 labeled with the organic fluorophore DY-485XL (a) and of the NK51-labeled matrix protein mthSp70 (b). (c) Overlay of the two images showing Tom20 in green and mthSp70 in red. (d) Excitation and absorption spectra for DY-485XL (dotted line) and NK51 (solid line). The two fluorophores are separated by subsequently exciting the sample at 488 nm (DY-485XL) and 532 nm (NK51). Both dyes are depleted by stimulated emission at 647 nm. (e) Reverse staining as a control (Tom20 with NK51 and Hsp70 with DY-485XL) yields similar results as the initial recording (c). Scale bars, 1 μm .

other parameters, these efficiencies are a function of the orientation of the fluorophore dipoles. Since dipoles that are oriented parallel to the x - y -plane are preferentially excited, the depletion efficiency of the z -component is usually less compared to other (lateral) components. Unlike other approaches⁵⁴, isoSTED-sdb microscopy accounts for this by using the z -component for spot compression along the z -axis where initial resolution is already best. Furthermore, the desired depletion pattern is readily produced without the need of complex beam shaping. Still, the depletion efficiencies are a function of the orientation of the fluorophores (among other parameters), which is a sample characteristic. This renders isoSTED-sdb imaging applicable to a subset of samples, where conditions are favorable.

To enable isoSTED-sdb imaging, the isoSTED microscope was modified according to (**Fig. 2.17a**). To potentially exploit a beneficial rotational diffusion of excited fluorophores, the existing STED lasers were replaced by a single erbium fiber laser (ELP-5-775-DG, IPG Photonics Corporation, Oxford, MA, USA) that emitted especially long pulses of 1 ns pulse length at a repetition rate of 20 MHz and a wavelength of $\lambda_{\text{STED}} = 775$ nm. A new excitation lightsource (PDL 800-B with LDH-P-C 635b, PicoQuant, Berlin, Germany), emitting pulses at $\lambda_e = 635$ nm, was installed in order to support dyes that match the red-shifted λ_{STED} .

The performance of the modified system was assessed by measuring fluorescent beads (Crimson, Molecular Probes) of different sizes (**Fig. 2.18a,b**). At a depletion power of $P_{\text{STED}} = \sim 49$ mW, a near-isotropic resolution (aspect ratio 1.4) of 30 nm (axial) and 21 nm (lateral) was achieved. To demonstrate isoSTED-sdb imaging of biological samples, histone clusters within the nucleus of an intact cell were immuno-labeled with a fluorescent dye (ATTO 647N, Atto-Tec, Siegen, Germany) and visualized by the recording of an optical x - z -section (**Fig. 2.18c**).

2.4.5 Discussion and outlook

An important advantage of the 4Pi-like isoSTED arrangement is that, for symmetry reasons, it inherently cancels the focal fields of all the STED beams in the geometric focal point, regardless of their polarization. This attribute facilitated the conceptually flawless implementation of a 3D zero with linearly and circularly polarized light, that advantageously addresses the molecules irrespective of their orientation in the focal plane and enables the single beam depletion scheme.

Instead of polarization, one could have also resorted to wavelength differences for forming the STED_{xy} and STED_z focal patterns. However, such a scheme would have made it challenging to identify the specific cavity path

2 A spherical nanosized focal spot unravels the interior of cells

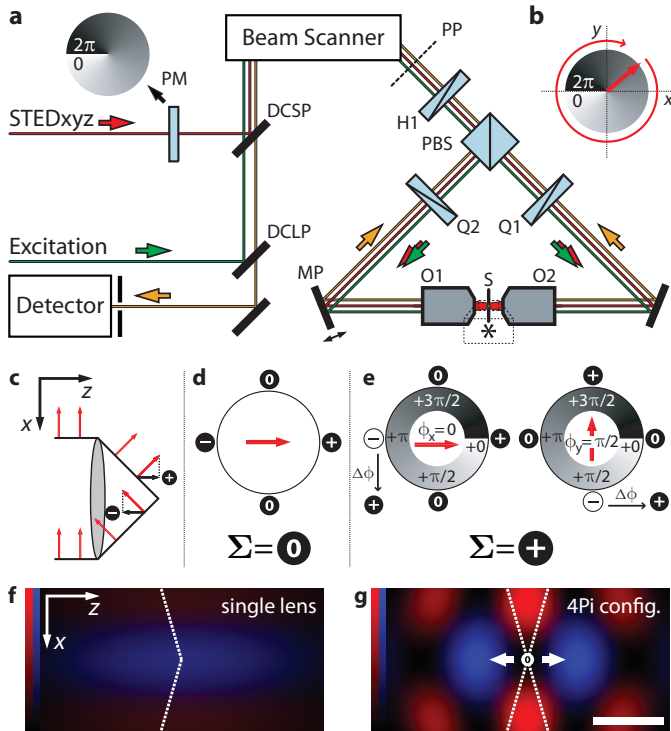


Figure 2.17: isoSTED-sdb microscope and PSF generation. (a) In this variant of isoSTED microscopy, two mutually orthogonal quarter-wave retarders (Q1, Q2) are inserted in each cavity arm and replace the half-wave retarder (H2, Fig. 2.11a) of the isoSTED microscope, resulting in circularly polarized excitation and depletion. (b) The orientations of Q1 and Q2 are tuned such that the lateral field vector of the depletion beam counterrotates with respect to the previously imprinted phase ramp. (c) Origin and direction of the z-component of the focal field of a single lens that is illuminated with a plane wave (linear) x-polarized light. The orientation of the z-component (small black arrows) of the electrical field vector (red arrows) is symbolized by '+' and '-' icons. (d) Schematic view of the back aperture of a single objective lens, illuminated with linear polarized (red arrow) light. (+/-/0)-icons mark positive, negative and vanishing contribution (z-strengths) of the specific quadrants to the z-component of the field at the focal center. Without a phase mask employed, the z-strengths cancel out, ($\Sigma(0, +, 0, -) = 0$). (e) Situation for circularly polarized light and a phase ramp as in (b). Two diagrams show the x- and the y-component separately, with relative phases $\phi_x = 0$ and $\phi_y = \pi/2$. Negative z-strengths are phase shifted by a total of $\Delta\phi = \pi$ which turns them positive. The results is a build-up of net z-strength at the focal center ($\Sigma = +$). (f) Focal intensity distribution for lateral (x, y, red) and axial (z, blue) field components in a focus that is generated as described in (e). The dotted line denotes the angular aperture of the lens. Maximum total intensity is reached at the focal center. (g) Focal intensity distribution as in (f), but for two opposing lenses in a 4Pi configuration with a 4Pi phase of 0. Because of the inverted z-direction of the second lens, the z-contributions of both lenses cancel out at the focal center (0), 'pushing' the intensity into two distinct maxima above and below the focus (arrows). The result is a sphere of light that surrounds the focal spot and allows for its 3D compression. Color tables of (f) and (g) are normalized to the same common maximum. Scale bar, 250 nm.

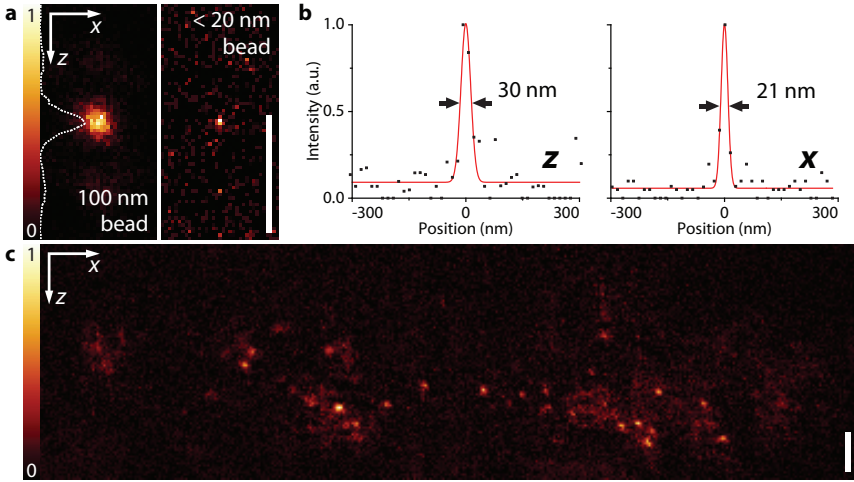


Figure 2.18: Experimental isoSTED-sdb PSF and imaging in the nucleus. (a) isoSTED-sdb recording of a 100 nm fluorescent bead as a probe for out-of-focus residual intensity. The z-profile shows less than 13 % residual intensity at side-maxima. (b) isoSTED-sdb recording of a <20 nm fluorescent bead. Gaussian fits through the z- and x- profile yield respective FWHM of 30 nm and 20 nm. To account for the low SNR, the amplitudes of the fitted functions were constrained to not exceed the value of the highest respective data point. The true FWHM are thus overestimated. (c) isoSTED-sdb recording of histone clusters in the nucleus of an intact cell. Scale bars, 500 nm.

difference that reconciles the formation of destructive interference for STEDz, constructive interference for STEDxy and constructive interference for the excitation light. In contrast, operating with the same λ_{STED} and a polarizing beamsplitter inherently provides the required relative phase difference.

In future, it will also be possible to resort to pulsed laser systems with noncoherent sequential pulses, making the use of two STED lasers obsolete. Further, photonic crystal devices and continuous wave lasers will greatly simplify future implementations of isoSTED microscopy. In any case, the scheme presented in this work (**Fig. 2.11, 2.17**) and its derivatives are rather definitive with regard to the general requirements for an optical system to compress a focal fluorescence spot by light. This is important because stimulated emission is just one way of reversibly inhibiting fluorescence. Other known mechanisms include the depletion of the fluorescence ground state^{11,12} and photoswitching of molecules between a fluorescent and a nonfluorescent state¹³. In all these cases, the resolution will follow the above equation determined by I_m/I_s , with I_s denoting the saturation intensity for the particular molecular mechanism. The latter can be lower than the values used for STED by several orders of magnitude.

In all variants of optical far-field fluorescence microscopy, the signal received from each sampling position contains unwanted contributions from outlying areas that manifest as background in the recorded image. Though mostly structureless, this background lowers the SNR and thereby limits the resolution obtained in the final data. A major advantage of a far-field optical method working with molecular ensembles is that the focal spot volume can be tuned in size by adjusting I_m/I_s , even during the imaging process. Further improvements should yield isotropic PSFs that are substantially smaller than the ~ 30 nm reported in this thesis. It should be feasible to generate focal spots whose shape and diameter can be continuously tuned in the nanometer range to accommodate the specific signal and resolution needs of the object to be investigated. This feature should be highly advantageous when translating the isoSTED concept to 3D imaging inside living cells. The fact that the presented data were obtained by implementing the isoSTED-cavity in a standard beam scanning confocal microscope underscores the potential of the isoSTED scheme for future applications in the life sciences and beyond.

3 Spotlights on isoSTED application

The development of isoSTED microscopy was aimed at furthering the understanding of biological organisms by providing a means to reveal the intricate structures found in nature. New fields of application open up where the design of novel nanomaterials demands insight into the laws of their formation. This is a brief overview of the present and upcoming applications of isoSTED technology.

3.1 Unfolding the blueprint of life

In cell biology, inseparable ties between structure and function manifest at all levels of organization. Starting on the scale of tissue, where the function of manifold specialized cell types reflects in their individual morphology, over intra-cellular organelles like the Golgi complex and the mitochondrion that separate the many consecutive steps of enzymatic reactions by an intricate compartmentalization, down to the structure of the biomolecules themselves that serve as building blocks of higher functionality.

To perform their functional and structural studies, biologist today can resort to a wide range of methods. Biochemical techniques give direct access to the interaction of biomolecules, but generally they lack sensitivity to spatial distributions and therefore rely on the isolation and separation of the structures of interest to characterize their constituents. Fluorescence microscopy became the method of choice due to its unmatched ability to precisely localize specific proteins, and because of its suitability for studying living cells. Its limited 3D-resolution however prevented it from being applicable to the imaging of complex structure at a scale below the wavelength of light. Taking advantage of the much shorter wavelength of the electron, electron microscopic (EM) approaches enable the visualization of labeled structures and surrounding membranes with nanometer resolution. Yet the low labeling density and the lacking preservation of the ultra structure rendered immuno EM to be unsatisfactory for the analysis of spatial protein distributions. With the development of isoSTED, light microscopy takes a wide step to narrow the gap in resolu-

tion towards that of EM, which makes it possible to readdress many previously unanswerable questions.

3.1.1 The Golgi apparatus

Named after its Italian discoverer Cammillo Golgi (Nobel prize in 1906 for his work on the nervous system), the Golgi apparatus is the central transshipment center of a cell. Its main function is the glycosylation of lipids and proteins, which labels them for transport to their respective destinations within the cell. Lysosomal proteins for example are marked by the attachment of mannose 6-phosphate (M6P), which binds to the M6P receptor of transport vesicles that are bound for lysosomes⁵⁵.

To facilitate the tagging of a vast number of molecule species, the Golgi apparatus consists of several subcompartments that (spatially) separate different sets of enzymes which act upon cargo molecules in sequence. These subcompartments, termed cisternae, are arranged in stacks, one side facing the endoplasmic reticulum (ER) where cargo is acquired, the other side facing the cytoplasm, where processed cargo is released onboard (transport/carrier) vesicles. Apart from this linear organization, the number of cisternae and the general morphology of Golgi stacks varies widely between cell lines. To become independent of the absolute number of cisternae, one has established a coordinate system that, if somewhat arbitrarily, divides a Golgi stack along the transport axis into three sections of equal extensions. Starting with the ER facing section, cisternae (within these sections) are assigned to the 'cis-', 'mid'- and 'trans'-Golgi. Cargo transport takes place along this cis-trans-axis, but the details are still a topic of debate. The cisternal maturation model⁵⁶ explains cargo transport with the movement of cisternae. Contrarily, the vesicular transport model⁵⁷ views the Golgi as a static structure in which vesicles transfer the cargo between cisternae. A recent third fundamental model proposes short-lived tubular connections⁵⁸ between cisternae as mode of transport.

A valuable contribution to the evaluation of these models can be expected from the direct imaging of the Golgi sub-structure, as exemplified by isoSTED imaging of the Golgi proteins GM130 and Giantin in human glioma cells (U373MG, human glioblastoma). GM130 is a cisternal matrix protein that mediates the binding of vesicles to the membranes of the cis-Golgi⁵⁹. Giantin has been shown to colocalize⁶⁰ with Galactosyltransferase which is located on the trans side⁶¹ of the Golgi apparatus. Two-color recordings of x-y-sections (**Fig. 3.1a,b**) show GM130 outlined by Giantin, a strong indication of a highly folded Golgi apparatus with local cis-trans-axes of varying directions. This shape reflects in a high resolution isoSTED recording (**Fig. 3.1c**) where the GM130 signal from separated cisternae forms distinct double structures.

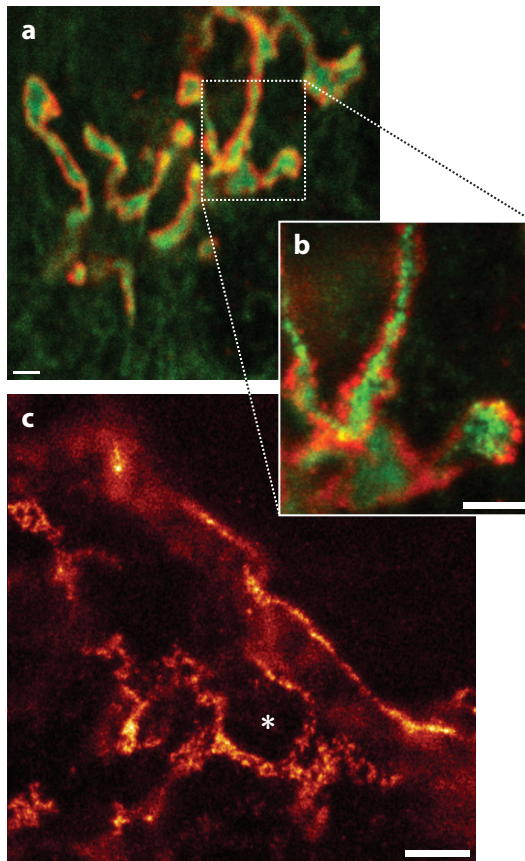


Figure 3.1: Sub-structure of the Golgi apparatus. (a) Dual-color confocal recording of the cis-Golgi protein GM130 (green) and the trans-Golgi protein Giantin (red). (b) isoSTED recording of the area marked in (a). Giantin clearly delineates GM130, indicating a high degree of folding. (c) A single color high resolution isoSTED image of cisternae labeled with GM130 visualizes their structure. Note the distinct features near (*). isoSTED data has been deconvolved. Scale bars, 1 μm .

3.1.2 Mitochondria

The cell's power house they are called; mitochondria are an essential part of all eucariotic organisms. By converting energy out of sugar and fat into the formation of adenosine triphosphate (ATP), they provide the cell with a universal energy carrier that serves as fuel for its metabolism. Mitochondria are tiny rod-shaped organelles, yet together they synthesize a gross 60 kg of ATP per day in a human body. Since they are occupied in a large variety of anabolic and catabolic processes, mitochondria also play an important role in several diseases, ranging from neurological⁶², over metabolic⁶³ and muscular diseases⁶⁴, right up to cancer⁶⁵.

As a former independent procariote, Mitochondria evolved into a specialized compartment that builds up a dynamic network within eucariotic cells. The individual tubules exhibit an outer diameter of around 300 nm and a complex interior that is divided into several reaction rooms (**Fig. 3.2a**): The smooth mitochondrial outer membrane surrounds the entire organelle. At contact sites this membrane is connected to the highly folded inner membrane, which in turn is organized into two contiguous but morphologically distinct domains; the cristae membrane and the inner boundary membrane. The functional composition of the mitochondrial membranes is only poorly understood, although the proteins within these membranes are very well characterized. Too little is known on their distribution, a topic that henceforth shall be addressed (**Fig. 3.2**.)

As an exemplary study, four proteins were imaged that fulfill diverse tasks within the mitochondrion, including protein import and ATP production. The mitochondrial proteom consists of about 1000 proteins, and though a small number of these ($\sim 1\%$) is still encoded by the mitochondrial mtDNA and is locally assembled inside the mitochondrion, most of its genome has been relocated to the host cell. The consequence is heavy traffic of inbound proteins at the entry gate^{49,50,51} of the outer mitochondrial membrane, the translocase of the outer membrane (Tom) complex. To physically fit through this gate, incoming proteins arrive in an unfolded and therefore unfunctional precursor state. They are recognized by the Tom70, Tom20 (**Fig. 2.15**) and Tom22 (**Fig. 3.2b**) receptor subunits and incorporated into the mitochondrion, where molecular chaperones such as the mitochondrial heat shock protein 70 (mtHSP70, **Fig. 3.2c**) aid the newcomer's transition into its final conformation. As another representative of chaperones, Cyclophilin D (**Fig. 3.2d**) is not associated with protein import and uniformly distributed in the mitochondrial matrix.

Being encoded by the nuclear genome, the subunits of the ATP-synthase complex (e.g. F_1F_0 ATPase(α), **Fig. 3.2e**) arrive at the mitochondrion as described above. Fully assembled, it is a molecular motor in the inner membrane, that builds up ATP from adenosine diphosphate (ADP) and an additional

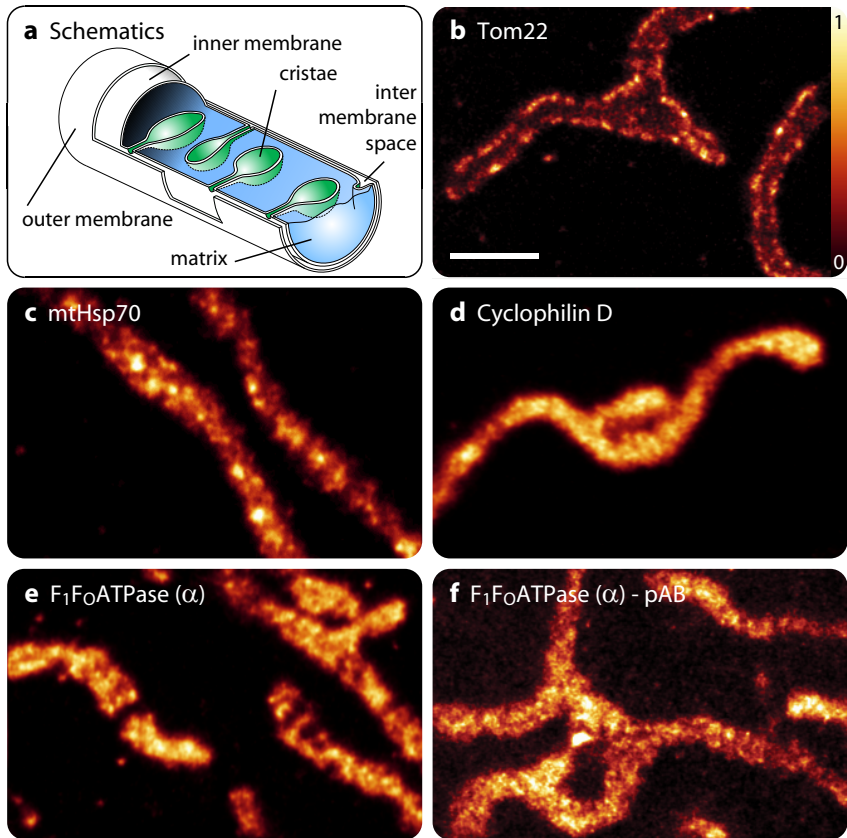


Figure 3.2: Spatial distribution of mitochondrial proteins. (a) Schematics of a mitochondrion. (b) isoSTED recording of Tom22 clusters in the outer membrane, (c) import associated mtHSP70, (d) Cyclophilin D located in the matrix, and (e) α -subunit of the ATP-synthase complex located in the inner membrane. (f) ATP-synthase as in (e), imaged with enhanced resolution by means of higher STED saturation and primary antibody labeling. Samples (b-e) were prepared according to methods (App. A). Images show deconvolved data. Scale bar, 1 μm .

phosphate group. To function, it needs a driving force that is generated in a sequence of enzymatic reactions, starting with cytoplasmic glycolysis and the oxidation of fatty acids. The citric acid cycle transfers the gained energy to electrons, which travel along the 'respiratory chain' of protein complexes and power its hydrogen-pumps. These transmembrane proteins push protons across the inner membrane, from the matrix into the intermembrane space, creating a electrochemical proton gradient. The ATP-synthase finally taps this stored energy by allowing a controlled back flow of protons which literally makes the motor spin. Depending on the specific organism, it generally takes between 3 to 5 protons to produce a single molecule of ATP.

Synergies between the development of improved microscopes and labeling techniques that account for the decreasing size of the focal spot will further advance resolution (**Fig. 3.2f**) and aid in the refinement of our understanding of mitochondria.

3.2 Studies on the architecture of nanomaterials

Nanomaterials feature order on a scale between molecular and microscopic structures. This order can entail astonishing material properties, a famous example is the immense tensile strength of carbon nanotubes that exceeds⁶⁶ 100 GPa, translating into the ability to endure a weight of over 10 t on a cable with a cross section of 1 mm². Block copolymers (BCPs), as another class of nanomaterials, are already found in various industrial products such as upholstery foam and asphalt additives. An intriguing aspect is their ability to self-assemble into a vast tapestry^{67,68,69,70,71} of complex (3D) structures. Since these structures mostly lie beyond the capabilities⁷² of conventional patterning techniques such as lithography and nanografting, BCPs can serve as templates⁷² for the construction of advanced nanostructures, e.g. in microelectronics⁷³. Due to the palette of parameters involved, control of structure formation is challenging though, and tools that allow the unambiguous mapping of the 3D structure assume crucial importance.

A BCP consists of two or more polymeric chains that are chemically different and covalently linked to each other. If the blocks are immiscible, enthalpy drives them to phase segregate, while entropic considerations promote mixing. The covalent connectivity of the blocks prevents complete separation and under appropriate conditions, a balance of thermodynamic forces drives the segregation into a variety of ordered structures. The equilibrium structure minimizes the unfavorable contact between the blocks without overstretching the chains and each block occupies portions on opposite sides of an interface known as the inter-material dividing surface (IMDS). The geometry adopted by the IMDS

and hence the morphology of the microstructure created depends on a variety of factors including the number of blocks, the degree of polymerization, volume fractions of the components, the extent to which the segments are incompatible, and the molecular architecture of the components. In real space, imaging of BCP structure has typically been performed with either electron or scanning probe microscopes. However, these techniques do not provide easy access to truly 3D structure information, since they either yield a 2D projection of thin sections, or are restricted to studies of near surface morphology. Recent efforts requiring the determination of complete 3D structures have thus concentrated on the use of confocal microscopy^{74,75}. However, the diffraction limited resolution of the confocal microscope restricts its use to the imaging of polymers of ultrahigh molecular weight that form sufficiently large structures. Since viscosity and relaxation time scale with the third power of the molecular weight, general interest clearly tends towards lighter and thus smaller and faster polymers that are of greater relevance for industrial applications.

In order to image the morphology of a block copolymer using high resolution isoSTED fluorescence microscopy, it is necessary to obtain contrast between the various phases present. This can be achieved either by exploiting marked variations in the spectral properties of the fluorophores in the different microdomain environments or by localizing the fluorescent species within specific microdomains. Potential strategies for the localization of the fluorescent species include the direct incorporation of the dye into the chain of one of the blocks during the synthesis of the BCP, the utilization of the preferential solubility of the fluorescent species in a particular phase, or the subsequent staining of the desired phases through either physical or chemical bonds. Here the latter strategy was successfully applied to facilitate isoSTED imaging of a poly(styrene-*b*-2-vinylpyridine) (PS-P2VP) block copolymer: A solution of polystyrene and poly-2-vinylpyridine of equal molecular weight ($m = 190$ kD each) was spin cast onto a coverslip to create a thin film of BCP. The sample was then solvent annealed to obtain phase separation, after which a fluorescent dye (ATTO 647N, Atto-Tec) was chemically bound to the P2VP phase. Embedding of the sample followed the procedure for a dye layer (**App. A**). isoSTED imaging revealed distinct polymer phases forming a laminar structure with a typical separation of 140 nm between two P2VP layers (**Fig. 3.3**).

These images of block copolymer nanostructures are notable for the possibilities that they create. The ability to obtain morphological information within the bulk of the sample, with microdomain specificity, in a non-invasive manner coupled with the demonstrated ability of isoSTED microscopy to achieve fast scanning will enable numerous fundamental studies. Examples of structural studies include the unambiguous mapping of the architecture of multicomponent BCPs, the imaging of the structural nature of defects, and the effect of

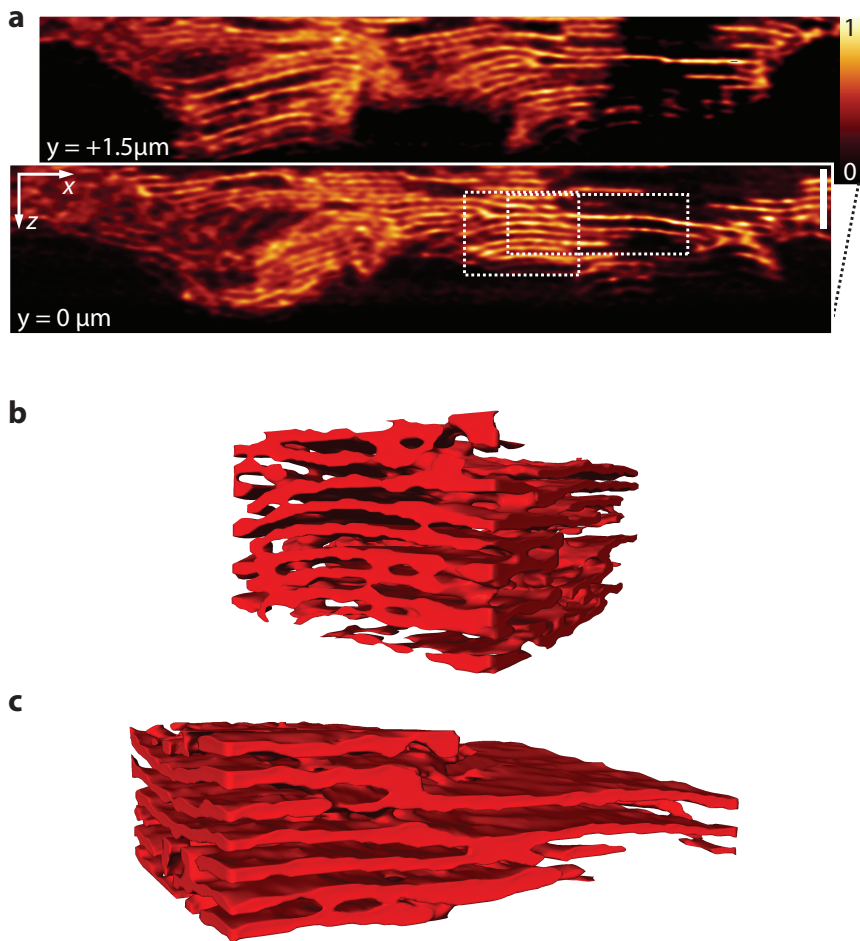


Figure 3.3: Non-invasive 3D imaging of PS-P2VP nanostructure. (a) Optical x-z-sections through an annealed film of PS-P2VP block copolymer reveal the distinct P2VP-lamellae within. The shown data is part of a deconvolved 3D stack. (b,c) 3D structure at defect locations. Two subsets of the data ((b) $\sim 2 \times 3 \times 1.5 \mu\text{m}^3$ and (c) $\sim 3 \times 2.5 \times 1 \mu\text{m}^3$, marked by frames in (a)) were processed by a segmentation algorithm and subsequently rendered. Scale bar, $1 \mu\text{m}$.

three dimensional confinement on BCP morphology. Dynamic studies could include elucidation of the mechanisms and dynamics behind the process of ordering in self assembly under various driving forces such as electric fields and graphoepitaxy. It is thus reasonable to anticipate that fluorescence nanoscopes will join electron microscopes and x-ray scattering instruments to become an important tool for polymer scientists.

A Methods

Sample preparation for water-immersion.

For PSF measurements, 10 μl of a 1:10,000 diluted suspension of fluorescent beads (yellow-green, specified diameter 100 nm, 2 % solids in distilled water, Molecular Probes, Eugene, OR, USA) were applied onto a coverslip. After drying, the sample was covered with a drop of water.

Live bacteria, *Escherichia coli*, were incubated with Oregon Green succinimidyl ester (O6147, Molecular Probes, Eugene, OR, USA) for 10min. After washing, the stained bacteria were attached to a cover slip with 0.1 % (w/v) poly-L-lysine in water (Sigma-Aldrich Chemie GmbH, Steinheim, Germany) and embedded in PBS (137 mM NaCl, 3 mM KCl, 8 mM Na_2HPO_4 , 1.5 mM KH_2PO_4 , pH 7).

Sample preparation for oil-immersion.

For PSF measurements, 10 μl of a 1:10,000 diluted suspension of fluorescent beads (Nile red, specified diameter 21 nm, 2 % solids in distilled water, Molecular Probes, Eugene, OR, USA) were applied onto a coverslip. After drying, the sample was covered with a thin layer of 97 % (v/v) 2,2'-Thiodiethanol (TDE) in PBS solution (refractive index $n = 1.515$ at room temperature)⁷⁶ and a second coverslip. Finally, the sample was sealed with nail polish.

For measurements of the z -response, clean coverslips were incubated with 1 % (v/v) 3-Aminopropyl (diethoxy) methylsilane in toluene under constant stirring for 30 min. Subsequent washing with water and 10 min incubation with 1 μM NK51 NHS-ester (Atto-Tec GmbH, Siegen, Germany) in DMSO solution yielded a fluorescent layer of NK51 dye that was bound to the coverslip. After a final wash, the sample was covered with a thin layer of oil (Immersion oil type B, $n_D = 1.515$, Cargille Laboratories, Cedar Grove, NJ, USA) and a second coverslip, and finally sealed with nail polish.

For immunolabeling, cultured Vero cells from the African green monkey, *Chlorocebus sp.*, were grown on coverslips, fixed with 8 % formaldehyde in PBS for 3-10 minutes at 37°C, extracted with 0.5 % (v/v) Triton-X-100 in PBS, blocked with 5 % BSA in PBS and incubated with a polyclonal rabbit antiserum against Tom20 (Santa Cruz Biotechnology, Santa Cruz, CA, USA) or with mouse monoclonal antibodies against mtHsp70 (mortalin/GRP 75, Ab-

cam, Cambridge, UK). The primary antibodies were detected with secondary antibodies (sheep anti-mouse, goat-anti-rabbit) that were custom-labeled with NK51 (AttoTec, Siegen, Germany) or DY-485XL (Dyomics GmbH, Jena, Germany). For the single color recoding of Tom20 (**Fig. 2.15**), custom labeled tertiary antibodies (donkey anti-goat; Jackson ImmunoResearch Laboratories, West Grove, PA, USA) were utilized to intensify the brightness of the detected structures. After labeling, an exchange of the buffer by a dilution series of TDE in PBS as described⁷⁶ resulted in a final embedding medium of 97 % TDE in PBS ($n = 1.515$). This embedding strategy greatly improves the optical properties of the sample and therefore prevents that local refractive index changes hamper resolution⁷⁶. The samples were covered with a second coverslip that was sparsely coated with fluorescent beads (Nile red, specified diameter 110 nm, SpheroTec Inc., Libertyville, IL, USA), to facilitate the initial alignment of the microscope, and finally sealed with nail polish.

B Publications and presentations

J. Bewersdorf, R. Schmidt & S.W. Hell

“Comparison of I⁵M and 4Pi microscopy.”

Journal of Microscopy **222**, 105-117 (2006).

R. Schmidt, C.A. Wurm, S. Jakobs, J. Engelhardt, A. Egner & S.W. Hell

“Spherical nanosized focal spot unravels the interior of cells.”

Nature Methods **5**, 539-544 (2008).

R. Schmidt et al.

“isoSTED microscopy with a single depletion beam.”

(in preparation)

R. Schmidt et al.

“Mitochondrial protein distributions.”

(in preparation)

R. Schmidt et al.

“Direct 3D imaging of block copolymer nanostructures.”

(in preparation)



Beam scanning 4Pi microscopy

Roman Schmidt, Jörg Bewersdorf, Stefan W. Hell

Department of NanoBiophotonics
Max-Planck-Institute for Biophysical Chemistry
37077 Göttingen, Germany



4Pi microscopy: sharpen the focus

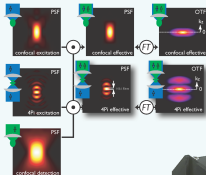


Figure 1: The effective point spread function (PSF) of a microscope (red color) is given by the product of its excitation and detection PSFs (left column). In 4Pi microscopy, excitation is by coherent addition of the wavefronts from two opposing objective lenses. The resulting intensity now forms a focal spot that is four to seven times smaller than that of a conventional confocal microscope. This leads to an improvement in axial resolution as can be seen in the corresponding Fourier transforms of the PSFs (optical transfer function, OTF). The support of the 4Pi OTF extends far beyond the confocal one along the axial axis, showing the transmission of higher spatial frequencies (right column).

Enhancing the 4Pi OTF

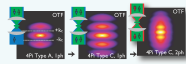
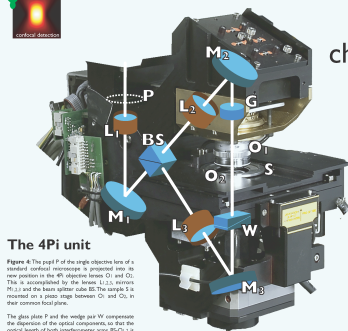


Figure 2: By using coherent excitation only (4Pi Type A), the OTF extends far beyond the confocal one along the axial axis, showing the transmission of higher spatial frequencies (right column).

Confocal laser scanning microscopy is the technique of choice for three-dimensional imaging of live biological cells. Since its resolution is limited by the numerical aperture of the objective lens used, a practical limit of about half a micron in the axial direction can not be exceeded. By coherent addition of the wavefronts from two opposing lenses, the 4Pi system offers a four to sevenfold improvement in the axial resolution down to $\sim 100\text{nm}$. A 4Pi beam scanning microscope has been recently developed in collaboration with Leica Microsystems that provides a stable and compact platform for biological experiments.

beam scanning: challenges and solutions



The 4Pi unit

Figure 3: The pair F of the single objective lens of a standard confocal microscope is projected into a new position in the 4Pi objective lens O and O_2 . This is accomplished by the lens L_1, L_2 mirrors M_1, M_2 and the beam splitter BS . The sample S is mounted on a piezo stage between O and O_2 in four corners (top plane).

The glass plate P and the wedge piezo W compensate the dispersion of the optical components, so that the optical length of both interferometer arms $BS-O_1$ is the same for all the wavelengths used.

Control of interferometric parameters

Table 1: The relative phase $\Delta\phi$ between both interferometer arms can be adjusted for a given drive using 4Pi unit. A pair of glass mirrors M_1, M_2 compensates the dispersion. This allows tuning of the system to realize Type C, contrast-interferometric interference (see below) to yield an optical OTF.

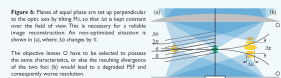
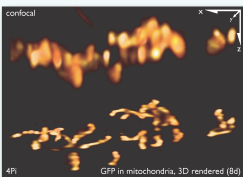
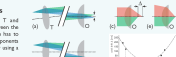


Figure 5: Phase of light planes on the sample. The light plane is tilted by θ so that it is kept constant with the field of view. This is necessary for a stable single concentration. An over-compensated situation is shown where $\Delta\phi$ changes by π .

The objective lenses O have to be selected to possess the same chromaticity, or else the resulting dispersion of the two foci (F) would lead to a degraded PSF and consequently worse resolution.

Preventing chromatic aberrations

Figure 6: Chromatic aberrations between both lenses L_1 and objective lens O leads to a lateral offset between the two foci for different wavelengths (λ), which has to be corrected by careful alignment of the components.

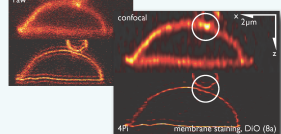


GFP in mitochondria, 3D rendered (8d)

the benefit: biological imaging with improved resolution

Figures 8a-d: Images of PC12 mammalian cells in standard confocal and 4Pi mode. The distinct shape of the 4Pi PSF lead to artefacts in the raw data ("ghost images"), that were restored by non-linear Richardson-Lucy deconvolution.

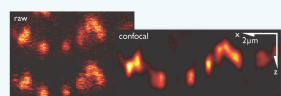
The setup consisted of a Leica SP2 with 4Pi unit, water immersion $63\times$ 1.2NA objective lenses and an Ar^+ -laser pumped Ti:Sa for 4Pi 2-photon excitation at 870nm , 1-photon excitation at 488nm was used in the confocal mode. Detection filters were set at 515nm .



membrane staining, DiO (8a)



GFP in mitochondria (8b)



GFP in mitochondria (8c)

Figure B.1: Canadian-German Workshop on Biophotonics, Ottawa, Canada, September 2004

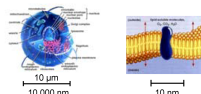


Fluorescence microscopy with <50 nm 3D resolution

NanoBiophotonics
MPI-BPC

A1

The aim of the project is to develop a focusing (i.e. far-field) fluorescence microscope with an isotropic 3D-resolution of <50 nm in (live) cells, operating with regular lenses and visible light. It is clear that such a tool will be a key device for quantitative investigations in the life sciences. Additionally, such a resolution will also facilitate the investigation of other samples, such as biological cells, colloids and complex fluids.

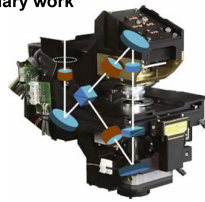
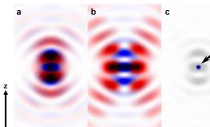


4Pi: PSF engineering

The effective point spread function (PSF) of a microscope is given by the product of its excitation and detection PSFs. In 4Pi microscopy, excitation is by coherent addition of the wavefronts from two opposing objective lenses, resulting in a focal spot that is four to seven times smaller than that of a conventional confocal microscope. This leads to an improvement in axial resolution, as can be seen in the corresponding Fourier transforms of the PSFs (optical transfer function, OTF). The support of the 4Pi OTF extends far beyond the confocal one along the optic axis, showing the transmission of higher spatial frequencies.



3D-STED-4Pi: Concept & Preliminary work



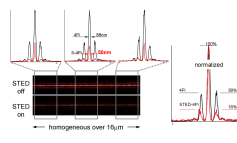
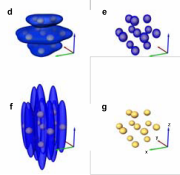
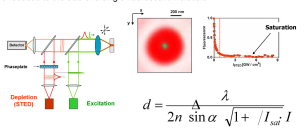
3D-STED-4Pi will exploit the 4Pi principle to create multiple simultaneous erase beams with the most narrow focal intensity distributions attainable, along the optical axis (a) and orthogonal (b). The resulting effective detection volume (c) will allow imaging of 3D structures below 50nm in size.

Below: An arbitrary structure (g) imaged with 4Pi (e), STED (f), and the proposed 3D-STED-4Pi (e).

Preliminary work for this project involved the construction of a 4Pi-Unit that can be mounted onto a commercial beam scanning microscope, thereby allowing sample selection and 4Pi-STED-imaging over a wide field of view.

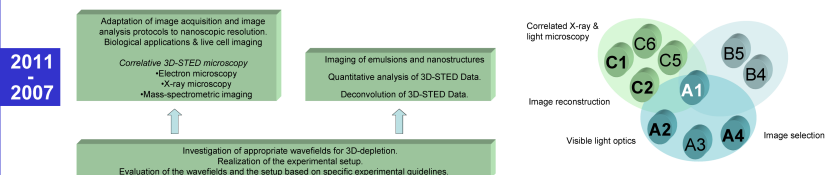
STED: Erasing fluorescence

A STED microscope reduces the effective detection volume by suppressing the fluorescence in the area around the focus by means of stimulated emission. This is usually done by overlaying the excitation volume with a donut-shaped erase beam that possesses zero intensity at the common focus. While this beam is still diffraction limited by itself, the non-linear intensity dependence of stimulated emission leads to a residual fluorescent area that – in theory – can be reduced to the size of a single fluorescent molecule.



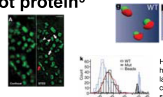
N51 layer, STED-4Pi Type C, excitation STED @ 514.965/647nm, 100x 1.4NA oil

3D-STED-4Pi: Schedule & Collaborations



2006 STED reveals organization of Bruchpilot protein⁵

The molecular organization of presynaptic active zones during calcium influx-triggered neurotransmitter release is the focus of intense investigation. The protein Bruchpilot (BRP) was observed in donut-shaped structures centered at active zones of neuromuscular synapses by using subdiffraction resolution STED. The effects of BRP mutant active zones were investigated. Unlike confocal counterpart, STED microscopy revealed donut-shaped structures recognized by Nyx2.



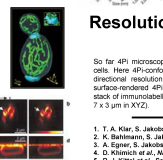
4Pi gives insight into hearing process⁴

2005

Hearing relies on faithful synaptic transmission at the ribbon synapse of cochlear inner hair cells (IHCs). At present, the function of presynaptic ribbons at these synapses is still largely unknown. 4Pi elucidates the co-localization (g. h) of the presynaptic ribbon component RIBEYE (green) and postsynaptic glutamate receptors GluR (red) and the size distribution (h). g. RIBEYE in wild-type IHCs and in ribbon-deficiency mutants.

2002 Fast multifocal 4Pi live cell imaging³

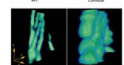
By introducing beam-scanning multifocal multiphoton 4Pi-confocal microscopy, fast fluorescence imaging of live cells with axial super-resolution is obtained. In conjunction with nonlinear image restoration, 3D imaging of live eukaryotic cells at an equispatial resolution of ~100 nm is demonstrated. Displayed is a surface-rendered 3D data stack of the mitochondrial network of S. cerevisiae (GFP-tagged mitochondrial matrix recorded with the MMA-4Pi).



Resolution improvement in aqueous samples by 4Pi²

2001

So far 4Pi microscopy was only possible in glycerol-mounted, fixed cells. Here 4Pi-confocal microscopy of aqueous objects with an all-directional resolution in the 100–200 nm range is presented: 3D surface-rendered 4Pi-confocal (a) and single lens confocal (b) data stack of immunolabeled mitochondrial network in fixed NIH3T3 cells (5 × 7 × 3 µm in XYZ).



2000 Diffraction barrier broken by STED microscopy¹

Resolution improvement by a factor of six along the z-axis in live cells is accomplished by quenching excited organic molecules at the rim of the focal spot through stimulated emission. 3D-images of a S. cerevisiae yeast cell with labeled vacuolar membranes with standard confocal resolution (a) and with axial resolution improved by STED (b). STED-XZ-images of membrane-labeled E. coli (c) and simultaneously recorded confocal image (c).



1. T. A. Klar, S. Jakobs, M. Dyba, A. Egner, S. W. Hell, *Proc. Natl. Acad. Sci. USA* 97, 8256 (2000)
2. K. Baumann, S. Jakobs, S. W. Hell, *Optics* 87, 155 (2001)
3. A. Egner, S. Jakobs, S. W. Hell, *Proc. Natl. Acad. Sci. USA* 99, 3372 (2002)
4. D. Klenning et al., *Nature* 434, 889 (2005)
5. R. J. Keller et al., *Science* 311, 1591 (2006)

Figure B.2: SFB755, Göttingen, Germany, March 2007

Bibliography

1. Hell, S. W. Double confocal microscope, (1992). EU Patent, No 0491289.
2. Hell, S. W. and Stelzer, E. H. K. Fundamental improvement of resolution with a 4Pi-confocal fluorescence microscope using two-photon excitation. *Opt. Commun.* **93**, 277–282 (1992).
3. Egner, A., Jakobs, S., and Hell, S. Fast 100-nm resolution 3D-microscope reveals structural plasticity of mitochondria in live yeast. *Proc. Natl. Acad. Sci. USA* **99**, 3370–3375 (2002).
4. Gugel, H., Bewersdorf, J., Jakobs, S., Engelhardt, J., Storz, R., and Hell, S. Cooperative 4pi excitation and detection yields 7-fold sharper optical sections in live cell microscopy. *Biophys. J.* **87**, 4146–4152 (2004).
5. Gustafsson, M., Agard, D., and Sedat, J. I⁵M: 3D widefield light microscopy with better than 100 nm axial resolution. *J. Microsc.* **195**, 10–16 (1999).
6. Hell, S. W. Improvement of lateral resolution in far-field light microscopy using two-photon excitation with offset beams. *Opt. Commun.* **106**, 19–24 (1994).
7. Hell, S. W. Increasing the resolution of far-field fluorescence light microscopy by point-spread-function engineering. In *Topics in Fluorescence Spectroscopy*, Lakowicz, J., editor, volume 5, 361–422. Plenum Press, New York (1997).
8. Hell, S. W. and Wichmann, J. Breaking the diffraction resolution limit by stimulated emission: STED. *Opt. Lett.* **19**(11), 780–782 (1994).
9. Klar, T. A., Jakobs, S., Dyba, M., Egner, A., and Hell, S. W. Fluorescence microscopy with diffraction resolution limit broken by stimulated emission. *Proc. Natl. Acad. Sci. USA* **97**, 8206–8210 (2000).
10. Dyba, M. and Hell, S. Focal spots of size $\lambda/23$ open up far-field fluorescence microscopy at 33 nm axial resolution. *Phys. Rev. Lett.* **88**, 163901 (2002).

11. Hell, S. W. and Kroug, M. Ground-state depletion fluorescence microscopy, a concept for breaking the diffraction resolution limit. *Appl. Phys. B* **60**, 495–497 (1995).
12. Bretschneider, S., Eggeling, C., and Hell, S. W. Breaking the diffraction barrier in fluorescence microscopy by optical shelving. *Phys. Rev. Lett.* **98**, 218103 (2007).
13. Hell, S., Jakobs, S., and Kastrup, L. Imaging and writing at the nanoscale with focused visible light through saturable optical transitions. *Appl. Phys. A* **77**, 859–860 (2003).
14. Gustafsson, M. G. L. Nonlinear structured-illumination microscopy: Wide-field fluorescence imaging with theoretically unlimited resolution. *Proceedings of the National Academy of Sciences of the United States of America* **102**(37), 13081–13086 (2005).
15. Rust, M. J., Bates, M., and Zhuang, X. Sub-diffraction-limit imaging by stochastic optical reconstruction microscopy (STORM). *Nat. Meth.* **3**, 793–796 (2006).
16. Betzig, E., Patterson, G., Sougrat, R., Lindwasser, O., Olenych, S., Bonifacio, J., Davidson, M., Lippincott-Schwartz, J., and Hess, H. Imaging intracellular fluorescent proteins at nanometer resolution. *Science* **313**(5793), 1642–1645 (2006).
17. Hess, S. T., Girirajan, T. P. K., and Mason, M. D. Ultra-high resolution imaging by fluorescence photoactivation localization microscopy. *Biophys. J.* **91**(11), 4258–4272 (2006).
18. Egner, A., Geisler, C., von Middendorff, C., Bock, H., Wenzel, D., Medda, R., Andresen, M., Stiel, A., Jakobs, S., Eggeling, C., Schnle, A., and Hell, S. W. Fluorescence nanoscopy in whole cells by asynchronous localization of photoswitching emitters. *Biophys. J.* **93**, 3285–3290 (2007).
19. Huang, B., Wang, W., Bates, M., and Zhuang, X. Three-dimensional super-resolution imaging by stochastic optical reconstruction microscopy. *Science Express* **319**, 810 – 813 (2008).
20. Fölling, J., Belov, V., Kunetsky, R., Medda, R., Schnle, A., Egner, A., Eggeling, C., Bossi, M., and Hell, S. W. Photochromic rhodamines provide nanoscopy with optical sectioning. *Angew. Chem. Int. Ed.* **46**, 6266–6270 (2007).

21. Westphal, V., Rizzoli, S. O., Lauterbach, M. A., Kamin, D., Jahn, R., and Hell, S. W. Video-rate far-field optical nanoscopy dissects synaptic vesicle movement. *Science* **320**(5873), 246–249 (2008).
22. Westphal, V., Kastrup, L., and Hell, S. W. Lateral resolution of 28 nm ($\lambda/25$) in far-field fluorescence microscopy. *Appl. Phys. B* **77**(4), 377–380 (2003).
23. Willig, K. I., Rizzoli, S. O., Westphal, V., Jahn, R., and Hell, S. W. STED-microscopy reveals that synaptotagmin remains clustered after synaptic vesicle exocytosis. *Nature* **440**(7086), 935 – 939 (2006).
24. Kittel, R. J., Wichmann, C., Rasse, T. M., Fouquet, W., Schmidt, M., Schmid, A., Wagh, D. A., Pawlu, C., Kellner, R., Willig, K. I., Hell, S. W., Buchner, E., Heckmann, M., and Sigrist, S. J. Bruchpilot promotes active zone assembly, Ca^{2+} -channel clustering, and vesicle release. *Science* **312**, 1051–1054 (2006).
25. Donnert, G., Keller, J., Wurm, C. A., Rizzoli, S. O., Westphal, V., Schnle, A., Jahn, R., Jakobs, S., Eggeling, C., and Hell, S. W. Two-color far-field fluorescence nanoscopy. *Biophys. J.* **92**(8), L67–69L (2007).
26. Egner, A. and Hell, S. W. Fluorescence microscopy with super-resolved optical sections. *Trends in Cell Biology* **15**(4), 207–215 (2005).
27. Denk, W., Strickler, J. H., and Webb, W. W. Two-photon laser scanning fluorescence microscopy. *Science* **248**, 73–76 (1990).
28. Bewersdorf, J. and Hell, S. Picosecond pulsed two-photon imaging with repetition rates of 200 and 400 MHz. *J. Microsc.* **191**, 28–38 (1998).
29. Hell, S. W., Lindek, S., Cremer, C., and Stelzer, E. H. K. Measurement of the 4pi-confocal point spread function proves 75 nm resolution. *Appl. Phys. Lett.* **64**(11), 1335–1338 (1994).
30. Gustafsson, M. G. L., Agard, D. A., and Sedat, J. W. Sevenfold improvement of axial resolution in 3D widefield microscopy using two objective lenses. *Proc. SPIE* **2412**, 147–156 (1995).
31. Gustafsson, M. G., Agard, D. A., and Sedat, J. W. 3D widefield microscopy with two objective lenses: experimental verification of improved axial resolution. In *Three-Dimensional Microscopy: Image Acquisition and Processing III*, Cogswell, C., Kino, G., and Wilson, T., editors, volume 2655, 62–66. *Proc. SPIE*, (1996).

32. Nagorni, M. and Hell, S. W. Coherent use of opposing lenses for axial resolution increase in fluorescence microscopy. I. Comparative study of concepts. *J. Opt. Soc. Am. A* **18**(1), 36–48 (2001).
33. Nagorni, M. and Hell, S. Coherent use of opposing lenses for axial resolution increase in fluorescence microscopy. II. Power and limitation of nonlinear image restoration. *J. Opt. Soc. Am. A* **18**(1), 49–54 (2001).
34. Richards, B. and Wolf, E. Electromagnetic diffraction in optical systems II. Structure of the image field in an aplanatic system. *Proc. R. Soc. Lond. A* **253**, 358–379 (1959).
35. Wolf, E. Electromagnetic diffraction in optical systems I. An integral representation of the image field. *Proc. R. Soc. Lond. A* **253**, 349–357 (1959).
36. Schönl, A. and Hell, S. Calculation of vectorial three-dimensional transfer functions in large-angle focusing systems. *J. Opt. Soc. Am. A* **19**(10), 2121–2126 (2002).
37. Hell, S. W., Schrader, M., Hänninen, P. E., and Soini, E. Resolving fluorescence beads at 100–200 nm distance with a two-photon 4Pi-microscope working in the near infrared. *Opt. Commun.* **117**, 20–24 (1995).
38. Hänninen, P. E., Hell, S. W., Salo, J., Soini, E., and Cremer, C. Two-photon excitation 4pi confocal microscope: Enhanced axial resolution microscope for biological research. *Appl. Phys. Lett.* **66**, 1698–1700 (1995).
39. Richardson, W. H. Bayesian-based iterative method of image restoration. *J. Opt. Soc. Am.* **62**, 55–59 (1972).
40. Born, M. and Wolf, E. *Principles of Optics*. Cambridge University Press, Cambridge, New York, Melbourne, Madrid, Cape Town, 7th edition, (2002).
41. Török, P., Varga, P., Laczik, Z., and Booker, G. R. Electromagnetic diffraction of light focused through a planar interface between materials of mismatched refraction indices: an integral representation. *J. Opt. Soc. Am. A* **12**(2), 325–332 (1995).
42. Lang, M. C., Staudt, T., Engelhardt, J., and Hell, S. W. 4Pi microscopy with negligible sidelobes. *New J. Phys.* **10**, 1–13 (2008).
43. Lang, M., Müller, T., Engelhardt, J., and Hell, S. W. 4Pi microscopy of type A with 1-photon excitation in biological fluorescence imaging. *Optics Express* **15**(5), 2459–2467 (2007).

44. Lanni, F. Standing-wave fluorescence microscopy. In Applications of Fluorescence in the Biomedical Sciences; Meeting, Pittsburgh, Pa., USA, Apr. 12-15, 1985., Taylor, D., editor, 505-522. Alan R. Liss, Inc., New York (1986). Meeting. Book. English.
45. Bailey, B., Farkas, D. L., Taylor, D. L., and Lanni, F. Enhancement of axial resolution in fluorescence microscopy by standing-wave excitation. *Nature* **366**, 44-48 (1993).
46. Freimann, R., Pentz, S., and Hrler, H. Development of a standing-wave fluorescence microscope with high nodal plane flatness. *J. Microsc.* **187**(3), 193-200 (1997).
47. Albrecht, B., Failla, A. V., Schweizer, A., and Cremer, C. Spatially modulated illumination microscopy allows axial distance resolution in the nanometer range. *Appl. Optics* **41**(1), 80-87 (2002).
48. Hell, S. W. Strategy for far-field optical imaging and writing without diffraction limit. *Phys. Lett. A* **326**(1-2), 140-145 (2004).
49. Hoogenraad, N. J., Ward, L. A., and Ryan, M. T. Import and assembly of proteins into mitochondria of mammalian cells. *Biochim. Biophys. Acta.* **1**(1592), 97-105 (2002).
50. Rehling, P., Brandner, K., and Pfanner, N. Mitochondrial import and the twin-pore translocase. *Nat. Rev. Mol. Cell Biol.* **5**, 519-530 (2004).
51. Neupert, W. and Herrmann, J. M. Translocation of proteins into mitochondria. *Annu. Rev. Biochem.* **76**, 723-49 (2007).
52. Dempster, A. P., Laird, N. M., and Rubin, D. B. Maximum likelihood from incomplete data via the EM algorithm. *J. Roy. Stat. Soc. B* **39**, 1-37 (1977).
53. Tsurui, H., Nishimura, H., Hattori, S., Hirose, S., Okumura, K., and Shirai, T. Seven-color fluorescence imaging of tissue samples based on fourier spectroscopy and singular value decomposition. *J. Histochem. Cytochem.* **48**, 653-662 (2000).
54. Bokor, N. and Davidson, N. Generation of a hollow dark spherical spot by 4 pi focusing of a radially polarized laguerre-gaussian beam. *Optics Letters* **31**(2), 149-151 (2006).
55. Sly, W. Receptor-mediated transport of acid hydrolases to lysosomes. *Curr. Top. Cell Regul.* **26**, 27-38 (1985).

56. Grassé, P. P. Ultrastructure, polarity and reproduction of Golgi apparatus. *Comptes Rendus de L'Academy des Sciences Paris* **245**, 1278–1281 (1957).
57. Jamieson, J. D. and Palade, G. E. Role of the Golgi complex in the intracellular transport of secretory proteins. *PNAS* **55**, 424–431 (1966).
58. Trucco, A., Polishchuk, R. S., Martella, O., Di Pentima, A., Fusella, A., Di Giandomenico, D., San Pietro, E., Beznoussenko, G. V., Polishchuk, E. V., Baldassarre, M., Buccione, R., Geerts, W. J. C., Koster, A. J., Burger, K. N. J., Mironov, A. A., and Luini, A. Secretory traffic triggers the formation of tubular continuities across golgi sub-compartments. *Nat. Cell Biol.* **11**, 1071–1081 (2004).
59. Marra, P., Maffucci, T., Daniele, T., Di Tullio, G., Ikehara, Y., Chan, E. K. L., Luini, A., Beznoussenko, G., Mironov, A., and De Matteis, M. The GM130 and GRASP65 Golgi proteins cycle through and define a subdomain of the intermediate compartment. *Nat. Cell Biol.* **3**, 1101–1113 (2001).
60. Schaub, B. E., Berger, B., Berger, E. G., and Rohrer, J. Transition of Galactosyltransferase 1 from trans-Golgi cisterna to the trans-Golgi network is signal mediated. *Mol. Biol. Cell* **17**, 51535162 (2006).
61. Rabouille, C., Hui, N., Hunte, F., Kieckbusch, R., Berger, E. G., Warren, G., and Nilsson, T. Mapping the distribution of Golgi enzymes involved in the construction of complex oligosaccharides. *J. Cell. Sci.* **4**(108), 1617–1627 (1995).
62. Kwong, J. Q., Beal, M. F., and Manfredi, G. The role of mitochondria in inherited neurodegenerative diseases. *J. Neurochem.* **97**, 1659–1675 (2006).
63. Nishikawa, T. and Araki, E. Impact of mitochondrial ROS production in the pathogenesis of diabetes mellitus and its complications. *Antioxid. Redox Signal.* **9**, 343–353 (2007).
64. Nishino, I., Kobayashi, O., Goto, Y.-I., Kurihara, M., Kumagai, K., Fujita, T., Hashimoto, K., Horai, S., and Nonaka, I. A new congenital muscular dystrophy with mitochondrial structural abnormalities. *Muscle. Nerv.* **21**, 40–47 (1998).
65. Brandon, M., Baldi, P., and Wallace, D. C. Mitochondrial mutations in cancer. *Oncogene.* **25**(34), 4647–4662 (2006).

66. Demczyk, B. G. Direct mechanical measurement of the tensile strength and elastic modulus of multiwalled carbon nanotubes. *Mater. Sci. Eng. A* **334**, 173178 (2002).
67. Park, M., Harrison, C., Chaikin, P. M., Register, R. A., and Adamson, D. H. Block copolymer lithography: Periodic arrays of $\sim 10^{11}$ holes in 1 square centimeter. *Science* **276**, 1401–1404 (1997).
68. Bates, F. S. and Fredrickson, G. H. Block copolymers - designer soft materials. *Phys. Today* **52**(2), 32–38 (1999).
69. Fink, Y., Urbas, A. M., Bawendi, M. G., Joannopoulos, J. D., and Thomas, E. L. Block copolymers as photonic band gap materials. *Lightwave Technol.* **17**(11), 1963–1969 (1999).
70. Stoykovich, M. P., Müller, M., Kim, S. O., Solak, H. H., Edwards, E. W., de Pablo, J. J., and Nealey, P. F. Directed assembly of block copolymer blends into nonregular device-oriented structures. *Science* **308**, 1442–1446 (2005).
71. Vriezema, D. M., Aragones, M. C., W., E. J. A. A., Cornelissen, J. J. L. M., Rowan, A. E., and Nolte, R. J. M. Self-assembled nanoreactors. *Chem. Rev.* **105**, 14451489 (2005).
72. Park, C., Yoon, J., and Thomas, E. L. Enabling nanotechnology with self assembled block copolymer patterns. *Polymer* **44**(22), 6725–6760 (2003).
73. Black, C. T., Ruiz, R., Breyta, G., Cheng, J. Y., Colburn, M. E., Guarini, K. W., Kim, H.-C., and Zhang, Y. Polymer self assembly in semiconductor microelectronics. *IBM Journal of Research and Development* **51**(5), 605–633 (2007).
74. Yoon, J., Lee, W., and Thomas, E. L. Highly oriented thin-film microdomain patterns of ultrahigh molecular weight block copolymers via directional solidification of a solvent. *Adv. Mater.* **18**(20), 2691–2691 (2006).
75. Lee, W. M., Yoon, J. S., Lee, H. J., and Thomas, E. L. Direct 3-D imaging of the evolution of block copolymer microstructures using laser scanning confocal microscopy. *Macromolecules* **40**, 6021–6024 (2007).
76. Staudt, T., Lang, M., Medda, R., Engelhardt, J., and Hell, S. W. 2,2-thiodiethanol: a new water soluble mounting medium for high resolution optical microscopy. *Microsc. Res. Tech.* **70**, 1–9 (2007).

Acknowledgment

This work was performed in the *Department of NanoBiophotonics* at the *Max-Planck-Institute for Biophysical Chemistry (MPI bpc)* in Göttingen. I would like to express my sincere appreciation and thanks to many people who have contributed to the success of this dissertation.

Prof. Dr. Stefan W. Hell, head of the department, envisioned fluorescence microscopy on the nanoscale and provided an outstanding scientific environment to work in this fascinating field. Numerous fruitful discussions and his ongoing encouragement have significantly contributed to the success of this thesis.

I would like to thank **Prof. Dr. Christoph Cremer** at the Kirchhoff Institute for Physics, University of Heidelberg, for his interest in my work and his willingness to be a referee of my thesis.

Furthermore I would like to thank **Dr. Alexander Egner**, *Department of NanoBiophotonics, MPI bpc*, for invaluable daily discussions, manyfold contributions and his dedication to this project, and **Dr. Jörg Bewersdorf**, formerly *Department of NanoBiophotonics, MPI bpc*, for his assistance during the initial stages, his competent advice and for showing me some tricks of the trade.

Interdisciplinary frontier research is a joint effort of sophisticated scientists. My thanks go to the present and former members of the following institutions for their close collaboration in an atmosphere of friendship. Individually I would like to thank:

From the research group *High Resolution Optical Microscopy, German Cancer Research Center*, Heidelberg: **Dr. Johann Engelhardt** for sharing his expertise in optical design and electronics.

From the research group of *Mitochondrial Structure and Dynamics, MPI bpc*, Göttingen: **Dr. Stefan Jakobs** for enlightening discussions about biology today. **Dr. Christian A. Wurm** for his dedication to the studies on mitochondria which manifested in many interesting samples.

From the *Department of NanoBiophotonics, MPI bpc*, Göttingen: **Jaydev Jethwa** for his technical assistance, especially with the water cooling and power electronics circuits, and for proof-reading of manuscripts. **Dr. Jan Keller** for competent programming support. **Rebecca Medda** for her counsel on biological samples. **Harald Meyer** for IT support. **Rainer Pick** for engineering

support. **Dr. Andreas Schönle** for helpful discussions and for providing the fabulous **IMSPECTOR** image analysis software. **Dr. Chaitanya Ullal** for introducing me into the intriguing world of block-copolymers.

Jonas Fölling, Dr. Benjamin Harke, Birka Hein, Annedore Punge and **Dr. Katrin I. Willig** for an enjoyable and inspiring office experience.

The people in our workshops did a great job in providing customized parts. **Wolfgang Kluge** and colleagues (optics) as well as **Rainer Schürkötter, Dieter-J. Czudnochowski, Bernd Henkner** and colleagues (mechanics) always found a way to realize even intricate microscope components.

My special thanks go to **Uurtsaikh Balchin** for moral support, and last but not least to my parents **Nada** and **Rudolf Schmidt** for constant support and always being there.

Göttingen, September 2008